Tertiary lymphoid structures are associated with enhanced macrophage activation, immune checkpoint expression and predict outcome in cervical cancer.

Laurent Gorvel[1,2,*], Marylou Panouillot[3], Marie-Sarah Rouvière[1,2], Emilien Billon[2], Stéphane Fattori[1], Jumaporn Sonongbua[1], Nicolas Boucherit[1,2], Amira Ben Amara[1,2], Olivia Quilichini[5], Samuel Granjeaud[7], Clara Degos[1], Jacques A. Nunes[1], Xavier Carcopino[6], Eric Lambaudie[5], Anne-Sophie Chretien[2], Renaud Sabatier[4,8], Marie-Caroline Dieu-Nosjean[3] and Daniel Olive[1,2*].

Affiliations :

1: Immunity and Cancer Team, Cancer Research Center of Marseille, CRCM, INSERM U1068, CNRS UMR7258, Aix-Marseille University U105, Marseille, France

2: Immunomonitoring Platform, Cancer Research Center of Marseille, CRCM, INSERM U1068, CNRS UMR7258, Aix-Marseille University U105, Marseille, France

3: UMRS1135 Sorbonne University, INSERM U1135, Centre of Immunology and Microbial Infections (Cimi), Immune Microenvironment and Immunotherapy Team, Paris, France

4: Predictive Oncology Laboratory, Cancer Research Center of Marseille, CRCM, INSERM U1068, CNRS UMR7258, Aix-Marseille University U105, Marseille, France

5: Department of Surgical Oncology, Institut Paoli-Calmettes, Marseille, France

6: Department of Obstetrics and Gynecology, Hôpital Nord, APHM, Aix-Marseille University (AMU), CNRS, IRD, IMBE UMR 7263, 13397, Marseille, France

7: CRCM Integrative Bioinformatics Platform, Cancer Research Center of Marseille, CRCM, INSERM U1068, CNRS UMR7258, Aix-Marseille University U105, Marseille, France

8 : Department of Medical Oncology, Institut Paoli-Calmettes, Marseille, France

*corresponding authors

All correspondences should be addressed to:

Laurent Gorvel, Ph.D, Cancer Research center of Marseille, 27 Bd Lei Roure, 13009 Marseille, France @ : laurent.gorvel@inserm.fr, tel : +33 4 86 97 72 75.

Or Daniel Olive, M.D., Ph.D., Cancer Research center of Marseille, 27 Bd Lei Roure, 13009 Marseille, France. @ : daniel.olive@inserm.fr, tel : +33 4 86 97 72 75

Abstract

Background Cervical tumors are usually treated using surgery, chemotherapy, and radiotherapy, and would benefit from immunotherapies. However, the immune microenvironment in cervical cancer remains poorly described. Tertiary lymphoid structures (TLS) were recently described as markers for better immunotherapy response and overall better prognosis in cancer patients.

Methods We integratedly evaluated the cervical tumor immune microenvironment, and specifically TLS importance, using combined high-throughput phenotyping, soluble factor dosage, spatial interaction analyses, and statistical analyses.

Results We demonstrate that TLS presence is associated with a more inflammatory soluble microenvironment, with the presence of B cells as well as more activated macrophages and dendritic cells (DCs). Furthermore, this myeloid cell activation is associated with expression of immune checkpoints, such as PD-L1 and CD40, and close proximity of activated conventional DC2 to $CD8^+$ T cells, therefore indicating better immune interactions and tumor control. Finally, we associate TLS presence, greater B cell density, and activated DC density to improved progression-free survival, and present it as an additional prognostic marker.

Conclusion To conclude, our results provide an exhaustive depiction of the cervical tumor immune microenvironment where TLS presence marks cell activation and immunotherapy target expression. These findings provide predictive clues for patient response to targeted immunotherapies.

Keywords Tertiary Lymphoid structures, Cervical cancer, Macrophages, Immune microenvironment.

Significance TLS maturation stratifies cervical cancer patients and associates with improved prognosis. TLS associate with the expression of immune checkpoints, notably in the macrophage compartment, which may represent a new therapeutic strategy.

58 **Introduction**

59 Cervical cancer is the fourth most common cancer in women and is still a public health issue in
60 developing countries (1). Cervical tumors are human papillomavirus (HPV)-positive in more than 95% of
61 cases. Vaccination against HPV provides good protection against the development of cervical tumors;
62 however, vaccination rates remain low worldwide (50% in both Europe and the USA)(1). Most cervical
63 tumors comprise well-infiltrated squamous cell carcinomas (SCC), the rest being less-infiltrated
64 adenocarcinomas (ADK)(2). Cervical SCCs are usually associated with better overall survival (OS) than
65 ADKs (5-year OS rates of 80% and 60%, respectively). Tumor severity is defined by International
66 Federation of Gynecology and Obstetrics (FIGO) stages, where a higher FIGO stage corresponds to worse
67 severity, lymph node (LN) invasion and metastasis, and correlates with poorer OS (decreasing to 55% at 5
68 years for FIGO stage IVa)(3).

69 Cervical tumors are treated using surgery and brachytherapy and chemotherapy. These are
70 debilitating treatments, especially for younger women in age to expect children. Immunotherapies
71 provide an advantageous set of treatment as they often present less toxicities than chemotherapy or
72 radiations. However, they require a well described immune environment, which is currently
73 understudied in cervical tumors. It is known that the T cell compartment harbors regulatory T cells
74 (Tregs), which are often associated with poor prognosis, and tumor-infiltrating conventional $CD4^+$ and
75 $CD8^+$ T cells, including HPV-specific T cells (4-6). The myeloid compartment is less well studied, with
76 research focusing on the Tumor-Associated Macrophage (TAM) infiltrate phenotype in the tumor bed
77 and how this associate with survival. Overall, whether they express CD163, CD206, or CD204, TAMs are
78 associated with advanced FIGO stages(7-10). Interestingly, the expression of programmed death-ligand 1
79 (PD-L1) by TAM is associated with programmed death-1 (PD-1) expression in the $CD8^+$ and $CD4^+$ T cell
80 compartments and improves prognosis when the ratio is in favor of $CD8^+$ T cell infiltrate (11-13).
81 However, most of these studies only correlate presence or absence of specific cell types to prognosis or
82 therapy response, and do not assess their spatial distribution within the tumor microenvironment.

83 Determining the localization and interactions of subsets of immune cells in the stroma, or within
84 the tumor nests is now critical to understanding tumor-specific treatment responses. Indeed, the
85 organization of the immune infiltrate, particularly into tertiary lymphoid structures (TLS), has been
86 associated with improved prognosis and response to immunotherapy in cancer patients (14). TLS are
87 organized aggregates of immune cells which develop at the site of chronic inflammation and display a
88 similar organization to lymphnodes (15). Indeed, TLS exhibit a B cell zone that includes mainly germinal

89 center B cells and follicular dendritic cells (FDCs), adjacent to a T cell zone comprising mainly T cells and
90 activated DCs (aDCs)(16,17). As TLS are heterogeneous, they warrant further investigation in specific
91 tumor microenvironments, as both their composition and the associated overall immune infiltrate may
92 provide insights for tumor-specific therapies and biomarkers(14). The presence of TLS within cervical
93 tumors has not been directly demonstrated yet and remains at the gene signature detection level(18).
94 However, TLS presence in HPV-positive head and neck SCCs (HNSCCs) is associated with a higher B cell
95 infiltrate and follicular helper T cells (Tfh)(19). A greater proportion of myeloid cells and $CD8^+$ T cells in
96 the vicinity of the TLS has also been reported. Together, these parameters are associated with an
97 improved prognosis in patients with HPV-positive HNSCC. Among the gynecological cancers, endometrial
98 tumors are reported to harbor TLS(20), and these are associated with improved prognosis in
99 microsatellite instability (MSI) endometrial tumors, allowing stratification for immunotherapy within this
100 patient group(20). Indeed, the improved prognosis seen in MSI patients suggests that the presence of
101 TLS and its associated immune infiltrate should be added to the molecular classification of endometrial
102 cancer(20).

103 Therefore, integrated investigation of the cervical tumor immune infiltrate is clearly warranted to
104 understand the different cellular compartments and their interactions. Here, we present an in-depth
105 study of TLS presence in the cervical cancer immune microenvironment and its impact on the overall
106 immune infiltrate, at both the cellular and spatial levels, and how these parameters may contribute to
107 overall prognosis and therapy response.

108

109 ## Methods

110 ### Human tumor samples

111 Human cervical tumor samples (n=34) were obtained from patients, who were included in the
112 prospective XAC-03 (NCT02875990) and GC-Bio-IPC (NCT01977274) clinical trials, conducted from 2013
113 to 2023. Patient follow-up was performed until December 2023 by assessing the occurrence of relapses
114 or death. The XAC-30 and GC-Bio_IPC trials were approved by the institutional review board (Comité
115 d'Orientation Stratégique (COS), Marseille, France) of the Paoli-Calmettes Institute and the Assistance
116 Publique des Hopitaux de Marseille (AP-HM), respectively. In accordance with the Declaration of
117 Helsinki, written informed consent was obtained from all patients.

118 Tumor samples were acquired prior to patients receiving any treatment. Healthy cervixes were
119 obtained from hysterectomies performed in cases of benign uterine pathologies (endometriosis and
120 fibroids). Before sampling and fixation, the cervix was assessed by a pathologist to confirm it was normal.
121 Clinical characteristics of the patients from whom samples were obtained are shown in **Table 1**. A list of
122 patient samples used in each experiment is available in **Suppl. Table 9**.

123

124 **Immunohistochemistry staining of FFPE slides**

125 All reagents and antibodies used for multiplex immunohistochemistry assay are listed in **Suppl.**
126 **Table 1–3**. After deparaffinization of two slides for e ach patient, epitope retrieval was performed with
127 the Dako Target retrieval solution (Dako) at pH 6.0 in a water bath for 30 minutes (min) at 97°C. After
128 washing with TBS (Euromedex), tissue sections were treated with 3% H_20_2 at room temperature (RT) for
129 15 min to inactivate endogenous peroxidase. After washing, sections were incubated with Protein Block
130 solution for 30 min at RT. To visualize TLS, tissue sections were incubated with anti-DC-Lamp and anti-
131 CD3 antibodies for one slide, and with anti-CD20 and anti-CD21 antibodies for a second slide. After
132 washing with TBS-0.04% Tween 20, the first slide was incubated with donkey $F(ab)'_2$ anti-rat IgG-biotin
133 and donkey $F(ab)'_2$ anti-rabbit IgG-alkaline phosphatase (AP), and the second slide with goat IgG anti-
134 mouse IgG2a-biotin and goat IgG anti-mouse IgG1-AP, for 30 min at RT. After washing steps, biotin-
135 conjugated antibodies were revealed with a streptavidin-horseradish peroxidase (HRP) solution,
136 incubated for 30 min at RT. CD3 and CD21 immunostaining revelations were performed by adding SAP
137 solution; DC-LAMP and CD20 were revealed with AEC solution. Slides were coverslipped with Glycergel
138 and scanned using a Nanozoomer scanner (Hamamatsu).

139

140 **Determination of TLS positive samples**

141 As described above, FFPE slides were stained for CD3, CD20, CD21 and DC-LAMP. B cells (CD20+)
142 inside B cell aggregates and activated DCs (DC-LAMP+) located in T cell (CD3+) aggregates were counted.
143 Their density was assessed by dividing B cell or activated DC count by the surface of the Tumor (in μm^2).
144 The obtained B cell and activated DC densities (in count/μm^2) were then scored by quartile, and
145 combined to assess TLS presence. A higher score for B cell and activated DC density resulted in higher
146 TLS score (quartile) and more formed TLS while a lower TLS score resulted in absence of TLS or

147 unorganized aggregates. TLS presence and maturity were then confirmed by microscopy by a trained
148 pathologist and CD21 staining marking Follicular DCs (FDCs) (**Suppl. Fig. 1, Table 2**).

149

150

151 **Immunofluorescence staining of FFPE slides**

152 For these experiments, 6 TLS^+ and 6 TLS^- cervical tumor FFPE slides were selected from the 34 total
153 samples. Selected samples had to exhibit the highest B cell and DC density scores in TLS^+ tumors and the
154 lowest scores in TLS^- tumors. To note, these samples were also analyzed by mass cytometry (CyTOF)
155 using the myeloid panel the lymphoid panel or both.

156 All reagents and antibodies used for multiplex IF assay are listed in **Supplementary Tables S1–3**.
157 Epitope retrieval was performed with the Target Retrieval solution at pH 6.0 or pH 9.0, depending on the
158 primary antibody tested. Slides were incubated in a water bath for 30 min at 97°C. After washing with
159 TBS, tissue sections were treated with 3% H_20_2 at RT for 30 min, washed again and incubated with
160 Protein Block solution for 30 min at RT. To visualize TLS, tissue sections were then incubated with anti-
161 DC-LAMP antibody for 1 hour at RT. After washing with TBS-0.04% Tween 20, tissue sections were
162 incubated with goat IgG anti-rat IgG1-HRP for 30 min at RT. After washing the tissue sections with TBS-
163 0.04% Tween-20, a tyramide conjugated to AF594 was incubated for 10 min at RT. After washing, the
164 tissue sections were incubated with the Target Retrieval solution for 10 min at 97°C. This step allowed
165 removal of the bound primary and secondary antibodies while protecting AF594 labeling of the DC-
166 $LAMP^+$ cells. It also enabled subsequent labeling of the same tissue sections with another antibody. The
167 other antibodies were tested after DC-LAMP labeling in the following order: anti-CD3 revealed with
168 $F(ab)'_2$ donkey anti-rabbit IgG-HRP and tyramide-CF514; anti-PanCk revealed with goat anti-mouse IgG1-
169 HRP and tyramide-AF488; anti-CD21 revealed with goat anti-mouse IgG1-HRP and tyramide-AF555; anti-
170 CD20 revealed with goat anti-mouse IgG2a-BV480; and anti-PNAd revealed with $F(ab)'_2$ goat anti-rat
171 IgGM-AF647.

172 To study the B cell, $CD8^+$ T cell, and myeloid compartments, three other IF panels were performed
173 using the same techniques and various antibody combinations: anti-CD1a revealed with goat IgG anti-
174 mouse IgG1-HRP and tyramide-CF514; anti-CD8 revealed with goat IgG anti-mouse IgG1-HRP, tyramide-
175 biotine and streptavidine conjugated to AF647; anti-CD68 revealed with goat IgG anti-mouse IgG1-HRP

176 and tyramide-CF430; anti-CD138 revealed with goat anti-mouse IgG1-HRP and tyramide-CF430; anti-
177 CD163 revealed with goat anti-mouse IgG1-HRP and tyramide-AF594.

178 Nuclei were then stained with DAPI for 5 min at RT before coverslips were mounted onto the glass slides
179 with Fluorescent Mounting Medium. Slide imaging was performed using a Zeiss Axio Observer Z1 at 385
180 nm, 430 nm, 475 nm, 511 nm, 555 nm, 590 nm and 630 nm with the corresponding filters and Zen
181 software (Zeiss).

182 **Spatial analysis of cervical tumor FFPE sections**

183 TLS quantification and density analysis were performed using HALO® software (Indica Labs). ROI
184 were delineated, and Hematies, Blank and Necrosis regions were excluded. A classifier was used to
185 discriminate TLS, tumor nest and stroma via staining of PanCk, CD20 and CD3. A Nuclei Segmentation
186 Artificial Intelligence algorithm allowed identification of cells based on their nuclei staining by DAPI (for
187 cell segmentation please see **Supp. Figure 1B**). A Multiplex IHC v3.2 analyzer was used to count $CD20^+$
188 and $DC\text{-}LAMP^+$ cells in immunohistochemistry slides. A HighPlex FL v4.2 analyzer was used to count cells
189 in IF slides. Spatial analyses with proximity analysis setup were used to measure the distance between
190 immune cell types.

191

192 **Tumor sample dissociation**

193 Tumor and healthy cervix samples were processed within 4 hours following surgery. Samples were
194 minced and then dissociated using a gentleMACS dissociator (Miltenyi Biotech) in RPMI 1640 culture
195 medium. Fragments were centrifuged and supernatants were frozen for soluble factor dosage.
196 Fragments were then suspended in Gentle Dissociation Solution (STEMCELL Technologies) and incubated
197 for 20 min at 37°C and 5% $C0_2$. Samples were again dissociated using the gentleMACS dissociator before
198 centrifugation and filtering through a 100 µm strainer. Finally, cells were counted and frozen in heat-
199 inactivated fetal calf serum 10% DMSO until staining.

200

201 **Soluble factor dosage**

202 *Chemokines, cytokines, and growth factors*

203 Supernatants were thawed at RT and used for growth factor, cytokines, and chemokines dosage by
204 Luminex using the 48-Plex pan-human cytokine kit (BioRad) according to the manufacturer procedure.
205 Briefly, supernatants were incubated with analyte-specific antibody-coated microbeads for 2 hours.
206 Supernatants were then washed and incubated with a PE labeled secondary antibody for MFI detection.
207 Data were acquired on a BioPlex-200 system (BioRad) and analyzed on BioPlex Manager 6.0 (BioRad),
208 comparing against standard curves for each analyte and according to manufacturer instructions. Raw
209 data were normalized against tumor sample weights (in grams).

210

211 *Immunoglobulins*

212 Supernatants were thawed at RT and used for IgG1-2-3-4, IgA, IgE, IgM and IgD dosage by
213 LEGENDplex (8 plex immunoglobulin isotyping panel, BioLegend) according to the manufacturer
214 procedure. Briefly, supernatants were incubated with analyte-specific antibody-coated microbeads for 2
215 hours. Supernatants were then washed and incubated with a PE-labeled secondary antibody for MFI
216 detection. Data were acquired on a LSRII (Becton-Dickinson) and Diva software and analyzed on
217 LEGENDplex data analysis software, comparing against standard curves for each analyte. Raw data were
218 normalized against tumor sample weights (in grams).

219

220 **Flow cytometry staining and acquisition**

221 Mononuclear cells were stained for live/dead Aqua, CD45-FITC, CD5-APC, CD19-PE-Cy7, CD20-PE-
222 Cf594, CD86-BV645, CD69-PE-Cy5.5, CD38-BV605, IgD-V450, CD27-BV785, CD21-BV711 and CD24-PE for
223 30 min at 4°C in PBS containing 2% FCS. Cells were then washed with PBS and fixed in 4% PFA for 20 min
224 at 4°C. After PBS washes, data were acquired on a LSRII (Becton-Dickinson). Marker expression was
225 compared against isotypic controls.

226

227 **Mass cytometry staining and acquisition**

228 Tumor cells were incubated with cisplatin (1 µM) to stain dead cells. Non-specific epitope binding was
229 blocked with 0.5 mg/mL human Fc Block (BD Biosciences, San Jose, CA, USA). Mononuclear cells were
230 stained for extracellular epitopes for 1h at 4°C, followed by permeabilization (FoxP3 permeabilization
231 reagent, eBioscience, San Diego, CA, USA) for 30 min at 4°C and intracellular marker staining with the

panels described in **Suppl. Tables 4–5**. Cells were then washed and labeled overnight with 125 nM iridium intercalator (Fluidigm, South San Francisco, CA, USA) in 2% PFA (Thermo-Fisher). Finally, cell pellets were suspended in Milli-Q water (Merck Millipore, Burlington, MA, USA) containing 10% EQ four element calibration beads (Fluidigm) and filtered through a 35 µm membrane before acquisition on a mass cytometer (Helios® instrument, Fluidigm). Mass Cytometry allows absolute quantification of cells by normalization against EQ™ Four Element Calibration Beads. The bead counts are known as well as the mean Di of all the masses. Beads are identified by 140Ce which is not used for antibody labelling. The normalization factor is the ratio of median Di values to EQ bead population median Di values of the encoding isotopes which cover an extensive portion of the mass range measurable on the Helios instrument. The normalization factors for mass channels between the encoding isotopes are linearly interpolated. All mass channel values for all events are then multiplied by these normalization factors to obtain the normalized values, and data is written to the normalized file. Absolute counts were normalized by weight of tumor (in grams) before comparison between samples.

Cytometry High-dimensional analysis

Flow cytometry analysis

B cell subsets were manually gated based on the expression of CD5, IgD, CD38, CD86, CD21, CD27, and CD24. This allowed the identification of Germinal center (GC) B cells, Memory B cells, Naïve B cells, Plasmablasts and pre-GC B cells. Memory B cells were also subdivided into activated memory, resting memory, intermediate memory and tissue like memory B cells. Subsets were quantified using FlowJo and statistical significance was assessed using one-way ANOVA, Kruskal Wallis test with Dunn's multiple comparison (GraphPad Prism). Absolute counts were normalized by weight of tumor (in grams) before comparison between samples.

Mass cytometry analysis

Myeloid cells ($CD45^{+}CD3^{-}CD19^{-}CD56^{-}CD33^{+}$) and T cells ($CD45^{+}CD3^{+}CD19^{-}CD33^{-}$) were manually gated, then exported using FlowJo (Becton-Dickinson). Data were arcsinh-transformed with a cofactor of 5. Myeloid and T cell populations were automatically defined using h-SNE, which allows a better clustering of rare populations such as tumor-infiltrating cells (using default settings of 30 perplexity and 1,000 iterations, Cytosplore V2.2.1)(21,22), and density clustering was analyzed. For myeloid cells,

262 CD11b, CD1c, CD1a, CD11c, HLA-DR, CD123, CD303, CD141, CD163, CD206, PD-L1, CD40, IL-6, and CD209
263 were used for clustering. For T cells, CD4, CD8, CD25, CD127, CTLA-4, PD-1, ICOS, CD69, CCR7, CD45RA,
264 and TIM3 were used for clustering.

265

266 **TLS associated myeloid cell population prediction**

267 Myeloid immune cell signature associated with TLS was created using Least Absolute Shrinkage
268 and Selection Operator (LASSO) regression to avoid overfitting due to a large number of parameters with
269 a limited number of patients (23). Myeloid cell populations that could predict TLS status were identified
270 among the 101 myeloid cell populations described by mass cytometry. Model was regressed on those
271 variables, with penalization and feature selection. Selected variables were then plotted according to TLS
272 status for representation. **Suppl. Table 6** shows the input parameters for the LASSO analysis. LASSO was
273 performed using RStudio V1.3.1093, R-4.0.3.

274

275 **Pagès Multiple factor analysis (MFA)**

276 To compare both clinical (FIGO 2018 classification, Age, LN, Emboli, Tumor size) and biological (DC
277 count, B cell count, DC density, B cell density, TLS) parameters we performed a Pagès Multiple factor
278 analysis (MFA), which determines the contribution of each parameter to the dimensions of a principal
279 component analysis. In our case it allowed to determine whether TLS and associated immune factors
280 were associated with negative parameters such as higher FIGO stage or lymphnode status or not. MFA
281 allows the comparison of both quantitative (DC count, B cell count, Age) and qualitative parameters (LN,
282 TLS, DC density, B cell density, FIGO, Tumor size, Emboli). FIGO I and II were grouped as a single variable
283 since only few stages I were available in our cohort. Hence, 3 groups were used for FIGO staging, FIGO
284 low (stages I-II, localized tumors), FIGO intermediate (int., stage III, LN invasion) and FIGO High (stage IV,
285 LN invasion and metastasis). Histology was separated in 2 groups, SCC and others (2 ADK and 1 Mixed
286 histology). B cell and DC densities were scored using quartiles, as we did for TLS maturation scoring. MFA
287 was performed using RStudio V1.3.1093, R-4.0.3. R scripts performing MFA are provided in **Suppl. File S1**
288 and input data are available in **Suppl. Table 7**.

289

290 **Multivariate analyses:**

291 A multivariate analysis was performed using the following parameters on the n=34 patient
292 samples, TLS^+ and TLS^-, FIGO stages low, int and high (similarly to those used for the MFA) and Histology
293 SCC and Others. These 3 parameters (7 variables) allow to statistically discriminated elements of better
294 or poorer prognosis, knowing that increased FIGO stages are of poor prognosis. Similarly, a multivariate
295 analysis was performed on the TCGA dataset using survival parameters, TLS- signature enrichment from
296 2 different articles (Goc + Coppola), tumor stages, lymphnode (LN) invasion, age and immune cell
297 population obtained from CIBERSORTx enrichment. Multivariate analysis was performed using RStudio
298 V1.3.1093.

299

300 **Cell enrichment analysis**

301 CIBERSORTx (Stanford University) was used for the immune cell enrichment analysis of the CESC
302 TCGA database. The individual gene expression file was uploaded to CIBERSORTx (24), and run using both
303 the relative and absolute modes, signature: LM22, 500 permutations, and disabled quantile
304 normalization (recommended for RNA-Seq data). For TLS scoring, enrichment scores for B cells, aDCs,
305 and $CD8^+$ T cells were scored as 1 (unenriched), 2 (poorly enriched), or 3 (highly enriched) by tiertile.
306 Noteworthy, the minimun enrichment score value considered usable by CIBERSORTx is 0.02. Samples
307 with high enrichment in every cell subset were considered TLS^+. Results from CIBERSORTx enrichment
308 are available in **Suppl. Table 8**.

309

310 **Statistical analysis**

311 TLS^- and TLS^+ tumors were discriminated by the morphology of T + B cell aggregates, their
312 presence *in situ*, and the quartile classification of B cell densities (1st quartile = 3.37 x 10^{-6} cells/µm²,
313 median = 3.31x10^{-5} cells/µm², 3rd quartile = 1.67.85 x 10^{-4} cells/µm²) and aDC densities (1st quartile =
314 70.19 x 10^{-6} cells/µm², median = 2.15x10^{-5} cells/µm², 3rd quartile = 4.85 x 10^{-5} cells/µm²). The 1st quartile
315 shows the lowest and the 4th quartile the highest densities. Aggregate presence and densities were then
316 scored according to the above-described parameters and tumors labeled as TLS^- and $TLS^{imm.}$ and $TLS^{mat.}$
317 (**Supp. Fig. 1**).

318 Statistical analyses were generated using GraphPad Prism V8.00, with data expressed as mean ±
319 standard error of the mean. Statistical significance between two groups was calculated using the non-

320 parametric Mann–Whitney test, while multiple group comparisons were calculated using the non-
321 parametric Kruskal-Wallis test followed by a Dunn, multiple comparison post-test. A p-value < 0.05 was
322 considered as significant. For survival analyses, PFS was defined as the time from diagnosis until death or
323 relapse, whichever occurred first. Patients without an event were censored at the time of their last
324 follow up. Survival times were estimated by the Kaplan–Meier method and compared using the log-rank
325 test.

326 **Results**

327 **TLS maturation levels vary in cervical tumors and is associated with soluble microenvironment**
328 **alterations.**

329 Cervical tumor samples (n=34) were screened for the presence of TLS according to CD20 (B cells),
330 CD21 (follicular dendritic cells, fDCs), CD3 (T cells) and DC-LAMP (activated DCs, aDCs) (**Fig. 1A**). First, B
331 cell aggregate presence were assessed by CD20 staining (**Supp. Fig 1A.**). B cell aggregates were then
332 associated with the presence of T cells ($CD3^+$) and aDCs ($DC\text{-}LAMP^+$). B cell and aDC density and the
333 presence of fDCs were then used as TLS maturation parameters. This allowed to divide our cohort into
334 TLS^- (no aggregates), TLS^{lo} (presence of lymphoid aggregates with low B cell and aDC density), immature
335 TLS ($TLS^{imm.}$, higher B cell and aDC density) and mature TLS ($TLS^{mat.}$, highest B cell and aDC density with
336 fDC presence) (**Fig. 1B, C and Supp. Fig 1A.**). We found $TLS^{imm.}$ or $TLS^{mat.}$ presence in 50% of our cohort
337 samples. TLS maturation stages were validated against manual TLS counts and showed increased TLS
338 counts in $TLS^{imm.}$ and $TLS^{mat.}$ samples (**Fig. 1D**). As B cell and aDC density did not vary between TLS^- and
339 TLS^{lo} samples, they were analyzed as a single group in the rest of the study and called TLS^-. **Fig. 1E**
340 displays a mature TLS exhibiting a B cell zone ($CD20^+$ B cell and $CD21^+$ FDC cluster) and a T cell zone ($CD3^+$
341 T cell and $DC\text{-}LAMP^+$ aDC cluster) and the presence of high endothelial venules ($PNAd^+$ cells). Next, we
342 measured secreted cytokines, soluble effectors and chemokines in $TLS^{mat.}$, $TLS^{imm.}$, TLS^- tumor and healthy
343 cervix dissociation supernatants by Luminex. CXCL1 was only significantly higher in $TLS^{mat.}$ samples
344 compared to healthy donors. IL-2ra, IL-16, CCL3, CXCL9 and CXCL10 were increased in $TLS^{mat.}$, $TLS^{imm.}$ and
345 TLS^- tumor supernatants compared to healthy cervix supernatants. CCL4, was increased in $TLS^{mat.}$ and
346 $TLS^{imm.}$ tumor supernatants compared to healthy cervix supernatants. TNF-α, TRAIL and CCL5 were
347 increased in $TLS^{imm.}$ and TLS^- tumor supernatants compared to healthy cervix supernatants, but not in the
348 $TLS^{mat.}$ supernatants. Overall, no significant differences were observed between $TLS^{mat.}$, $TLS^{imm.}$ and TLS^-
349 conditions (**Fig. 1F**). In summary, our results show that TLS are present in 50% of cervical tumors in our

350 cohort, are associated with higher densities of B cells and aDC, and tends to be associated with increased
351 CXCL1.

352

353 **TLS^+ tumors exhibit a higher B cell infiltrate characterized by an enrichment of plasmablasts in the**
354 **stromal compartment.**

355 We analyzed the B cell compartment in TLS^+ and TLS^- tumors by flow cytometry and unsupervised
356 analysis. B cell subsets were identified by manual gating according to the expression of CD19, CD20, CD5,
357 IgD, CD27, CD24, CD38 and CD21 (**Fig. 2A**). The absolute number of B cells, normalized by grams of
358 tumor sample, was higher in TLS^+ tumors as compared to TLS^- tumors (**Fig. 2B**). Germinal center B cells
359 (GC, $CD38^+IgD^-$), pre-GC ($CD38^+IgD^+$), Memory B cells ($CD38^-IgD^-$), naïve B cells ($CD38^-IgD^+$) or
360 plasmablasts ($CD38^{hi}IgD^-$) did not vary significantly between TLS^- and TLS^+ tumors (**Fig. 2C**). Among
361 memory B cells, we identified Tissue Like Memory B cells (TLM, $CD27^-CD21^-$), Intermediate memory B
362 cells ($CD27^-CD21^+$), resting memory B cells ($CD27^+CD21^+$) and activated memory B cells ($CD27^+CD21^-$).
363 None of these subset frequencies were significantly different in TLS^+ vs. TLS^- tumors (**Fig. 2D**). Hence, we
364 investigated the spatial localization of B cells within the cervical tumor and stroma by multiplex
365 immunofluorescence (IF) (**Fig. 2D)**. Briefly, we applied the tumor nest region of interest (ROI),
366 determined as pan-cytokeratin positive ($PanCk^+$), to 6 TLS^+ and 6 TLS^- samples. The absence of PanCk
367 staining identified the stroma ROI. Also, all immune cells were $PanCk^-$. We observed no significant
368 differences in $CD20^+CD138^-$ B cells, $CD20^+CD138^+$ plasmablasts, and $CD20^-CD138^+$ plasma cells between
369 TLS^- and TLS^+ samples in the tumor nest (**Fig. 2E**). While $CD20^-$ plasma cells and B cells infiltrate did not
370 vary, plasmablasts infiltrated TLS^+ stroma significantly more than TLS^- stroma (**Fig. 2F**). As plasmablasts
371 increased in TLS^+ stroma, we assessed soluble immunoglobulins (Ig) concentration in $TLS^{mat.}$, $TLS^{imm.}$, TLS^-
372 and healthy cervix supernatants, and found significant increases in IgG1, IgG2, IgG3, IgA, IgM and IgD in
373 $TLS^{mat.}$, $TLS^{imm.}$, TLS^- sample supernatants compared to those of healthy cervix (**Fig. 2G**). Here, we
374 observed no statistically significant differences between the TLS^-, $TLS^{mat.}$ and $TLS^{imm.}$ Samples. IgG4 was
375 solely significantly increased in $TLS^{mat.}$ tumors compared to healthy cervix. Interestingly, $TLS^{mat.}$ showed
376 increased levels of IgE compared to healthy cervix, TLS^- samples and a close to significant increase
377 compared to $TLS^{imm.}$ supernatants (p-val = 0.061). (**Fig. 2G**). Altogether, these results suggest enrichment
378 of the B cell compartment marked by enriched plasmablasts in TLS^+ tumors which may increases the
379 secretion of IgE.

380

381 **CD163$^+$ macrophages and activated cDC2 are enriched in TLS$^+$ cervical tumors**

382 The myeloid compartment is known to regulate TLS formation (macrophages)(25,26) and to participate
383 in their T cell-activation function (aDCs)(27). Therefore, we characterized the myeloid compartment by
384 mass cytometry and identified 8 clusters composed of Langerhans cells (LCs, CD1a$^+$CD11c$^+$), CD1a^{lo} DCs
385 (CD1c$^+$CD1a^{lo}), cDC1 (HLA-DR$^+$CD11c$^+$CD11b$^-$CD141$^+$), cDC2 (CD11c$^+$CD1c$^+$), pDCs (CD123$^+$CD303$^+$), early
386 myeloid-derived suppressor cells (eMDSCs, HLA-DR$^-$/^{lo}CD11b$^+$CD14$^-$CD15$^-$), monocytic MDSCs (mMDSCs,
387 HLA-DR$^{-/lo}$CD11b$^+$CD14$^+$) and TAMs (CD64$^+$CD68$^+$HLA-DR$^+$) (**Suppl. Fig. 2A, 1B**). We also divided TAMs
388 according to CD163 expression (**Fig. 3A; Suppl. Fig. 2A**). TAM numbers did not vary significantly between
389 TLS$^-$ and TLS$^+$ tumors. However, the frequency of CD163$^+$ TAMs was higher in TLS$^+$ tumors compared to
390 TLS$^-$ tumors (**Fig. 3B**). *In situ* analysis of TAMs showed a trend for increased CD163$^+$ TAM infiltrate in TLS$^+$
391 sample stroma and tumor (**Fig. 3C**). Next, we assessed the infiltration of TLS$^+$ and TLS$^-$ samples by cDC2,
392 LCs and CD1a^{lo} DCs, and observed an increased number of cDC2 in TLS$^+$ samples compared to TLS$^-$
393 samples (**Fig. 3D**). Therefore, we investigated cDC2 localization using the DC-LAMP marker for aDCs and
394 CD1a for LCs. We found no difference in aDCs (CD1a$^-$DC-LAMP$^+$), activated LCs (aLCs, DC-LAMP$^+$CD1a$^+$),
395 and immature LCs (iLCs, DC-LAMP$^-$CD1a$^+$) infiltrate in the tumor ROI (PanCk$^+$). However, aDCs infiltrate
396 was significantly higher in the TLS$^+$ sample stroma (**Fig. 3E**). In summary, our results show an increase in
397 CD163$^+$ macrophages and aDCs in the stroma of TLS$^+$ samples.

398

399 **Myeloid cells are more activated and better differentiated in TLS$^+$ tumors**

400 We investigated the phenotypic variations within myeloid cell subsets. We assessed the expression
401 of PD-L1, CD40, LILRB2, CD1d, CCR2, CCR5, CXCR4, CD80, CD86, HLA-DR, PVR, Nectin2, IL-6, CD10, CD206,
402 CD209 and CD141 among LCs, CD1a^{lo}DCs, cDC1, cDC2, pDCs, eMDSCs, mMDSCs, CD163$^-$ TAMs, and
403 CD163$^+$ TAMs. The frequencies were filtered on a 10% average expression and a minimum of 30 cells per
404 cluster. We analyzed the resulting 101 variables (44 TLS$^+$, 57 TLS$^-$) using the LASSO algorithm to obtain
405 each variable predictive of either a TLS$^+$ or TLS$^-$ profile (**Fig. 4A**). CD163$^+$ TAMs were the most highly
406 represented cell type in the TLS$^+$ group, with six of these variables corresponding to the contribution of
407 CD1d, CXCR4, PD-L1 and CCR5 (**Fig. 4B**; **Suppl. Table 6**). CD40 expression, which marks activation, on
408 cDC2 was also associated with the TLS$^+$ environment (**Fig. 4B**), which is logical considering that the
409 presence of aDCs is one of the main features of a TLS$^+$ microenvironment. Early MDSCs contributed to
410 the TLS$^+$ group with the expression of CCR2 (**Fig. 4C**). IL-6 expression on CD163$^-$ TAMs and CD1a^{lo} DCs
411 were also selected by the LASSO analysis (**Fig. 4C**). PVR$^+$CD1a^{lo} DCs (poliovirus receptor, TIGIT ligand) was

412 also selected by the LASSO algorithm. Finally, the presence of mMDSCs associated with a TLS$^-$
413 microenvironment (**Fig. 4C**). These findings were validated by a univariate analysis conducted as a post-
414 test. All variables associated with a TLS$^+$ microenvironment were significant, while only IL-6$^+$CD163$^-$ TAMs
415 were significant in a TLS$^-$ microenvironment (Log2FC>1 and *p*-val<0.05) (**Fig. 4D)**. Overall, the myeloid cell
416 contribution to a TLS$^+$ environment is determined by the expression of activation (CD40) and inhibition
417 (PD-L1) markers, which reflects a better differentiation of TAMs and cDCs. Furthermore, the contribution
418 of chemokine receptor expression (CXCR4, and CCR5) by TAMs also indicates an increase in the
419 recruitment of these cells. Finally, our results show the importance of the myeloid cell contribution to a
420 TLS$^+$ environment, which reflects a greater differentiation and activation of mainly macrophages, and
421 DCs.

422

423 **Spatial analysis reveals increased interactions between aDCs and CD8$^+$ T cells, which exhibit higher**
424 **diversity in TLS$^+$ tumors**

425 We hypothesized that the involvement of aDCs in TLS$^+$ tumors was associated with their proximity to
426 CD8$^+$ T cells, and could enhance immune response. Therefore, we performed cell segmentation and
427 identified aDCs (DC-LAMP$^+$CD1a$^-$), activated CD1a$^+$ DCs (aCD1a$^+$ DC, DC-LAMP$^+$CD1a$^+$), and CD8$^+$ T cells
428 **(Fig. 5A)**. Next, we quantified the number of CD8$^+$ T cells within a 10 µm, 10–20 µm and 20–30 µm range
429 of either a single aDC or aCD1a$^+$ DC (**Fig. 5B**). The number of CD8$^+$ T cells within a 10 µm, a 10–20 µm and
430 a 20–30 µm range of an aCD1a$^+$ DC tended to increase in TLS$^+$ compared to TLS$^-$ tumors, although the
431 difference was not significant (**Fig. 5C**). However, the number of CD8$^+$ T cells within a 10 µm range of an
432 aDC significantly increased in TLS$^+$ tumors compared to TLS$^-$ tumors (**Fig. 5D left**), and remained
433 unchanged in the 10–20 µm and 20–30 µm ranges. This close proximity suggests that aDCs directly
434 interact with CD8$^+$ T cells more efficiently in TLS$^+$ tumors, which may improve tumor control (**Fig. 5D**).

435 To further dissect the T cell response between TLS$^+$ and TLS$^-$ tumors, T cell subsets were mapped.
436 We showed that absolute numbers of naïve (CCR7$^+$CD45RA$^+$), central-memory (CM, CCR7$^+$CD45RA) and
437 effector-memory CD8$^+$ T cells (EM, CCR7$^-$CD45RA$^-$) were increased in TLS$^+$ tumors, which was not the case
438 for effector-memory re-expressing CD45RA (TEMRA, CCR7$^-$CD45RA$^+$) CD8$^+$ T cells (**Fig. 5E**). The absolute
439 numbers of CD4$^+$ T cell subsets also varied between TLS$^+$ and TLS$^-$ tumors. Indeed, naïve and TEMRA CD4$^+$
440 T cell numbers were increased in TLS$^+$ tumors (**Fig. 5F**). Therefore, these results show a greater diversity
441 and differentiation of the T cells and T cell response in TLS$^+$ tumors.

442 Using h-SNE clustering and density clustering, we identified variations due to specific marker and
443 quantified the cluster frequencies (**Fig. 5G, 5H**). Among $CD4^+$ T cells, only EM $CD4^+$ T cells varied. Indeed,
444 EM $CD4^+$ T cells which did not express any specific checkpoint marker (**Fig. 5G** "$Checkpoint^-$") and
445 $CD69^+CD127^+$ EM $CD4^+$ T cells were enriched in TLS- tumors compared to TLS^+ tumors (**Fig. 5G**). Among
446 $CD8^+$ T cells, one $CD69^+CD28^-PD\text{-}1^+$ EM $CD8^+$ T cells were enriched in TLS^+ tumors (**Fig, 5H**). In summary,
447 these results show increased aDC/T cell crosstalk and T cell activation and immune checkpoint
448 expression in TLS^+ tumors compared to TLS^- tumors.

449

450 **Mature TLS improve prognosis in cervical tumors.**

451 We hypothesized that the enhanced activation of immune cells within TLS^+ tumors could allow
452 patient segregation and predict progression-free survival (PFS). Therefore, we performed a Pages-
453 multiple factor analysis (MFA), which allows patient segregation by quantitative parameters (DC count, B
454 cell count, age) and qualitative parameters (FIGO stage, LN invasion, emboli presence, DC and B cell
455 density, TLS maturation, relapse and death, treatment), and assesses the impact of these parameters on
456 patient survival (**Supp. Fig. 3A, B**). The MFA defined two axes, where Dim.1 (Axis 1) corresponded to
457 immune parameters (TLS and immune cell counts) and Dim.2 (Axis 2) corresponded to disease-related
458 variables (Stages, Treatment) (**Supp. Fig. 3A, B**). LN invasion and emboli presence discriminated patient
459 along Dim.2, while DC and B cell number and densities discriminated patient along Dim.1 (**Supp. Fig. 3C**).
460 Age and Histology did not influence patient segregation (**Supp. Fig. 3C**). Here, we showed that patients
461 were well-segregated along Dim.1 by the different TLS maturation status, especially between mature TLS
462 and the two other groups (**Fig. 6, A**). FIGO stages and discriminated patients along Dim.2. Interestingly,
463 relapses and death segregated patients along Dim.1, and patient that relapsed or died corresponded
464 mainly to patients with immature TLS or not presenting TLS (**Fig. 6, A**). A multivariate analysis was
465 performed between presence or absence of TLS, FIGO stages and Histology and showed that high FIGO
466 stages were associated significantly with death and relapse (p-val = 0.009) while TLS presence tended to
467 associate to survival (p-val = 0.093) (**Suppl. Fig. 4, A**), which confirmed our results from the MFA.

468 Next, we studied patient PFS according to TLS^-, $TLS^{imm.}$ and $TLS^{mat.}$, and found that the $TLS^{mat.}$ group
469 (n=6 patients) did not include any death or relapse, while the $TLS^{imm.}$ (n=10 patients) included one death
470 and one relapse, and the TLS^- group (n=17 patients) included one death and four relapses (**Fig. 6B**). **Fig.**
471 **6C** shows better PFS in the $TLS^{mat.}$ group, and similar PFS curves in the $TLS^{imm.}$ and TLS^- groups. To validate
472 these results, we performed an immune cell enrichment analysis on the cancer genome atlas CESC

473 dataset (TCGA) using the CIBERSORTx algorithm (**Supp.Table 8**), followed by a survival analysis according
474 to B cell, $CD8^+$ T cell, activated DC (aDCs), and $CD4^+$ TEM enrichment. B cell and $CD8^+$ T cell enrichment
475 significantly improved patient survival, while aDCs only showed a non-significant trend for improved
476 survival and $CD4^+$ TEM enrichment did not influence survival outcome (**Supp. Fig. 3D**). Finally, we scored
477 the enrichment for TLS presence, where TLS^+ tumors are enriched for B cells, aDCs and $CD8^+$ T cells and
478 confirmed TLS^+ tumors association with better survival (**Fig. 6D**). To strengthen these results, we also
479 performed survival analyses using two published TLS-related gene signatures (from Coppola et al.(28)
480 **Fig. 6E** and Goc et al. (27) **Fig.6F**), which again showed better prognosis in patient with enriched TLS-
481 related gene signatures. We also performed a multivariate analysis on the TCGA cohort using TLS gene
482 signature enrichment from *Coppola et al.* and *Goc et al.* to avoid redundancy with CIBERSORTx individual
483 population enrichment, tumor stages (sSTAGEs), LN invasion, metastasis presence, and Age. Multivariate
484 analysis returned that plasmocytes, $CD8^+$ T cells and M2 macrophages significantly associated with
485 survival, which matched our results of stromal $CD138^+$ and $CD8^+$ T cell number increase, as well as
486 $CD163^+$ macrophages frequency. Expectedly, LN invasion and advanced tumor stages (T4) associated
487 with death (**Suppl.Fig 4,B**). TLS signatures did not associate with survival in this analysis. This may be due
488 to transcriptional signature being redundant with those used by CIBERSORTx enrichment, or critical
489 parameters lacking such as spatial organization and cell densities within TLS. In summary, mature TLS are
490 associated with improved PFS in cervical cancer.

491

492 **Discussion**

493 Our study demonstrates that TLS are associated with a more differentiated and activated immune
494 infiltrate in cervical tumors. Indeed, the presence of TLS is associated with better differentiation and
495 activation of macrophages and DCs, which is linked to a better $CD8^+$ T cell recruitment and activation.
496 Altogether, these parameters contribute to a better prognosis in patients with TLS^+ cervical tumors.
497 Although our cohort is of modest size, our results are robust and validated by multiple statistical
498 methods and unsupervised analyses. Furthermore, they integrate quantitative and qualitative methods,
499 which allows to assess the diversity of cervical tumor microenvironment.

500 Indeed, we used an integrated approach to investigate TLS and the immune infiltrate in cervical
501 tumors. First, we showed an increase in CXCL1 in $TLS^{mat.}$ TMEs specifically. CXCL1 is usually associated
502 with poorer prognosis in cervical tumors (29), however, the presence of mature TLS seems to

503 counterbalance this effect in our cohort. IL-16, TNF-α, IFN-α, CCL5, CXCL9 and CXCL10 are linked to TLS
504 and increase immune infiltrate and better prognosis in a transcriptomic signature(30). These soluble
505 effectors seemed to increase progressively with TLS maturation, but these changes remained not
506 significant, which may be due to the size of our cohort. IL-16 attracts $CD4^+$ T cells, but also macrophages
507 and DCs (31,32). CXCL9 and CXCL10 are produced in response to IFN-γ in the TME, participate to T cell
508 recruitment to hyperplastic epidermis via CXCR3 (33), and associate to prognosis improvement in
509 estrogen receptor-negative breast tumors(34), but promotes progression in tongue cancer(35). CCL5
510 allows T cell, immature DC and monocyte/macrophage recruitment(36,37), but also allows angiogenesis
511 and tumor growth (38), through the recruitment of macrophages (39), which could be prevented by
512 neutralizing the chemokine (40) or its signaling pathway(38).

513 Consequently, a TLS^+ microenvironment is associated with enriched immune cell proportions,
514 which is common among cervical cancer and other HPV^{+} [19] and HPV^- tumors(15,17,41,42). As expected,
515 the analysis of the B cell compartment showed an enrichment in overall B cells within TLS^+ samples.
516 More specifically, we found an increase in $CD138^+$ plasma cells within the stromal compartment of these
517 samples. Plasma cells were associated with cytokine production, chemotaxis and carcinogenesis in a
518 single cell RNA seq study of cervical tumors(43). In our study, plasma cell enrichment was associated
519 with an increased abundance of intra-tumoral IgEs and IgGs in TLS^+ samples. Tumor specific IgEs are
520 currently investigated as therapeutic strategies (44). Their relation with TLS^+ TME and activated
521 macrophages will be discussed in the adapted paragraph. To our knowledge, no previous studies exist on
522 the intra-tumoral IgE and IgG presence in cervical tumors. In cervical cancer, anti-HPV neutralizing IgGs
523 mark vaccination efficiency preventing HPV-induced malignancies (45). While natural HPV clearance only
524 allows protection against a specific strain of HPV and generates low IgG titers vaccination allows the
525 targeting of multiple HPV strains and are more abundant(46,47). Therefore, the increased presence of
526 intra-tumoral IgGs in TLS^+ tumors could be linked to a better response to HPV and/or tumor antigens,
527 which would contribute to improved prognosis in TLS^+ patients.

528 Myeloid cells contribute to the regulation of immune responses in tumors(48-52). aDC
529 infiltration is usually associated with a better T cell activation and overall better control of tumor
530 progression (53,54). Here, we show an enrichment of $CCR2^+CD40^+$ aDCs in TLS^+ samples compared to TLS^-
531 samples within cervical tumor and stroma. Here, CCR2 indicates an increased recruitment of aDCs from
532 the blood to the TME. In TLS^+ samples, aDCs accumulated in the stroma where they interact closely with
533 $CD8^+$ T cells. Similarly, Ruffin *et al.* demonstrated that cell-cell neighborhoods are composed of myeloid

534 cells, $CD8^+$ T cells, B cells, and conventional T cells in HNSCC tumors that exhibited mature GC^+TLS and
535 had improved prognosis (19). In ovarian tumors, the presence of antigen presenting cell niches where
536 $CD11c^+$ myeloid cells interact with $CD8^+$ T cells potentiates anti-CD28 therapy and improves
537 prognosis(55). By analyzing $CD8^+$ and $CD4^+$ T cell phenotypes we observed a more diverse infiltrate. EM,
538 TEMRA, naïve, CM $CD4^+$, and $CD8^+$ T cells were all enriched in TLS^+ tumors, while remaining at low levels
539 in TLS^- tumors.

540 TAMs are often associated with a negative outcome. Indeed, $CD204^+$, $CD206^+$ and $CD163^+$ TAMs
541 are associated with decreased prognosis in cervical cancer (48) and many other tumor types (56-59).
542 Here, we report an increase in the expression of immune checkpoints and ligands (PD-L1, CD40) and
543 chemokine receptors (CCR2 and CCR5) in TLS^+ tumors. CCR2 and CCR5 expression indicates the blood
544 monocyte origin of TAMs in TLS^+ tumors. TLS are known to improve response to immunotherapies(60,61)
545 which fits with an increased expression of immunotherapy targets, such as CD40, PD-L1, CCR2 and CCR5,
546 on TAMs and aDCs. This has been clearly established for immune checkpoint inhibitors such as anti-PD-1,
547 anti-PD-L1, and anti-CTLA-4(60,61). Recently, $PD\text{-}L1^+$ TAM were associated with $PD\text{-}1^+$ T cells, which
548 appeared to improve survival when the ratio is in favor of $CD8^+$ T cell infiltrate in cervical tumors (11-13)
549 and when $PD\text{-}L1^+$ TAMs were forming niches with T cells rather than being in contact with tumor cells in
550 breast tumors (62), which correspond to features of TLS^+ TMEs and our Cox regression results. Agonistic
551 anti-CD40 mAbs allow DCs to improve anti-tumoral responses (63-66). We observed increased
552 expression of CCR2 and CCR5 on TAMs from TLS^+ cervical tumors. Targeting these chemokine receptors
553 represent an innovative strategy to limit TAM infiltration. Indeed, CCR2/CCR5 inhibitors are currently
554 being investigated in colorectal and pancreatic cancers (67). In addition, the CCR5 inhibitor Maraviroc
555 improved the immune response in HNSCC and chordoma (39,68), while a CCR2 inhibitor in combination
556 with bevacizumab reduced tumor size in mouse models of ovarian cancer by inhibiting the MAPK
557 pathway (69). Interestingly, the activation of TAM also fits with an increased presence of IgE. Indeed,
558 anti-tumoral IgEs were shown to increase macrophage inflammatory properties and cytokine production
559 (70). This probably occurs to the FCεRI, which is used to identify TAMs (71). Taken together, the
560 increased expression of immunotherapy targets on myeloid APCs may offer more therapeutic options,
561 and their proximity to a greater $CD8^+$ T cell may potentiate the response to immunotherapies in TLS^+
562 tumors.

563 TLS maturation segregated patients into 3 distinct groups, TLS^-, $TLS^{imm.}$ and $TLS^{mat.}$, and were
564 logically associated with increasing B cell and DC densities and numbers. $TLS^{mat.}$ tumors were associated

565 with improved PFS, compared to $TLS^{imm.}$ and TLS^{-} tumors. These results are in accordance with previous
566 studies showing that TLS maturation is associated with better prognosis (15,41,72) and often helps
567 stratify patients when used as an independent prognostic marker (20) or therapy response marker
568 (60,61). Indeed, TLS presence has refined the molecular classification of patients with endometrial
569 tumors, by sub-stratifying those with MSI into an $MSI^{+}TLS^{+}$ patient group with improved prognosis (20).
570 In HNSCC, melanoma and sarcoma, B cell-alone mediated survival rates similar to those seen in TLS^{+}
571 tumors (19,60,61).

572 In conclusion, our results show that TLS in cervical cancer arise from a microenvironment which
573 is more prone to anti-tumoral response. Indeed, TLS^{+} tumors are enriched in B cells, aDCs, activated
574 macrophages and immune checkpoint positive T cells. Furthermore, activated DCs and macrophages
575 express a greater diversity of costimulatory molecules, are in close proximity of $CD8^{+}$ T cells, which
576 indicates a greater potential for T cell stimulation. Altogether, our results provide a comprehensive
577 characterization of the immune microenvironment in cervical tumors, in terms of phenotype, spatial
578 organization, and immune cell interactions. Furthermore, our results highlight that TLS are associated
579 with well-differentiated cells expressing immunotherapy targets, raising the possibility of TLS as a
580 predictive marker for patient response to specific therapies.

581

582 **References**

583 1. Sung H, Ferlay J, Siegel RL, Laversanne M, Soerjomataram I, Jemal A, *et al.* Global Cancer
584 Statistics 2020: GLOBOCAN Estimates of Incidence and Mortality Worldwide for 36 Cancers in
585 185 Countries. CA Cancer J Clin **2021**;71:209-49
586 2. Nayar R, Wilbur DC. The Pap test and Bethesda 2014. Cancer Cytopathol **2015**;123:271-81
587 3. Odicino F, Pecorelli S, Zigliani L, Creasman WT. History of the FIGO cancer staging system. Int J
588 Gynaecol Obstet **2008**;101:205-10
589 4. Tong WW, Shepherd K, Garland S, Meagher A, Templeton DJ, Fairley CK, *et al.* Human
590 papillomavirus 16-specific T-cell responses and spontaneous regression of anal high-grade
591 squamous intraepithelial lesions. The Journal of infectious diseases **2015**;211:405-15
592 5. Koskimaa HM, Paaso AE, Welters MJ, Grenman SE, Syrjanen KJ, van der Burg SH, *et al.* Human
593 papillomavirus 16 E2-, E6- and E7-specific T-cell responses in children and their mothers who
594 developed incident cervical intraepithelial neoplasia during a 14-year follow-up of the Finnish
595 Family HPV cohort. J Transl Med **2014**;12:44
596 6. Woo YL, van den Hende M, Sterling JC, Coleman N, Crawford RA, Kwappenberg KM, *et al.* A
597 prospective study on the natural course of low-grade squamous intraepithelial lesions and the
598 presence of HPV16 E2-, E6- and E7-specific T-cell responses. Int J Cancer **2010**;126:133-41

599 7. Cao L, Sun PL, He Y, Yao M, Gao H. Immune stromal features in cervical squamous cell carcinoma
600 are prognostic factors for distant metastasis: A retrospective study. Pathol Res Pract
601 **2020**;216:152751
602 8. Chen XJ, Han LF, Wu XG, Wei WF, Wu LF, Yi HY*, et al.* Clinical Significance of CD163+ and CD68+
603 Tumor-associated Macrophages in High-risk HPV-related Cervical Cancer. J Cancer **2017**;8:3868-
604 75
605 9. Guo F, Kong W, Zhao G, Cheng Z, Ai L, Lv J*, et al.* The correlation between tumor-associated
606 macrophage infiltration and progression in cervical carcinoma. Biosci Rep **2021**;41
607 10. Kawachi A, Yoshida H, Kitano S, Ino Y, Kato T, Hiraoka N. Tumor-associated CD204(+) M2
608 macrophages are unfavorable prognostic indicators in uterine cervical adenocarcinoma. Cancer
609 Sci **2018**;109:863-70
610 11. Colbert LE, El MB, Lynn EJ, Bronk J, Karpinets TV, Wu X*, et al.* Expansion of Candidate HPV-
611 Specific T Cells in the Tumor Microenvironment during Chemoradiotherapy Is Prognostic in
612 HPV16(+) Cancers. Cancer Immunol Res **2022**;10:259-71
613 12. Li L, Ma Y, Liu S, Zhang J, Xu XY. Interleukin 10 promotes immune response by increasing the
614 survival of activated CD8(+) T cells in human papillomavirus 16-infected cervical cancer. Tumour
615 Biol **2016**
616 13. Hanna BS, Llao-Cid L, Iskar M, Roessner PM, Klett LC, Wong JKL*, et al.* Interleukin-10 receptor
617 signaling promotes the maintenance of a PD-1(int) TCF-1(+) CD8(+) T cell population that sustains
618 anti-tumor immunity. Immunity **2021**;54:2825-41 e10
619 14. Schumacher TN, Thommen DS. Tertiary lymphoid structures in cancer. Science
620 **2022**;375:eabf9419
621 15. Fridman WH, Meylan M, Petitprez F, Sun CM, Italiano A, Sautes-Fridman C. B cells and tertiary
622 lymphoid structures as determinants of tumour immune contexture and clinical outcome. Nat
623 Rev Clin Oncol **2022**;19:441-57
624 16. Dieu-Nosjean MC. Tumor-Associated Tertiary Lymphoid Structures: A Cancer Biomarker and a
625 Target for Next-generation Immunotherapy. Adv Exp Med Biol **2021**;1329:51-68
626 17. Sautes-Fridman C, Lawand M, Giraldo NA, Kaplon H, Germain C, Fridman WH*, et al.* Tertiary
627 Lymphoid Structures in Cancers: Prognostic Value, Regulation, and Manipulation for Therapeutic
628 Intervention. Front Immunol **2016**;7:407
629 18. Lin Z, Huang L, Li S, Gu J, Cui X, Zhou Y. Pan-cancer analysis of genomic properties and clinical
630 outcome associated with tumor tertiary lymphoid structure. Sci Rep **2020**;10:21530
631 19. Ruffin AT, Cillo AR, Tabib T, Liu A, Onkar S, Kunning SR*, et al.* B cell signatures and tertiary
632 lymphoid structures contribute to outcome in head and neck squamous cell carcinoma. Nat
633 Commun **2021**;12:3349
634 20. Horeweg N, Workel HH, Loiero D, Church DN, Vermij L, Leon-Castillo A*, et al.* Tertiary lymphoid
635 structures critical for prognosis in endometrial cancer patients. Nat Commun **2022**;13:1373
636 21. Ben Amara A, Rouviere MS, Fattori S, Wlosik J, Gregori E, Boucherit N*, et al.* High-throughput
637 mass cytometry staining for deep phenotyping of human natural killer cells. STAR Protoc
638 **2022**;3:101768
639 22. van Unen V, Hollt T, Pezzotti N, Li N, Reinders MJT, Eisemann E*, et al.* Visual analysis of mass
640 cytometry data by hierarchical stochastic neighbour embedding reveals rare cell types. Nat
641 Commun **2017**;8:1740
642 23. Kang J, Choi YJ, Kim IK, Lee HS, Kim H, Baik SH*, et al.* LASSO-Based Machine Learning Algorithm
643 for Prediction of Lymph Node Metastasis in T1 Colorectal Cancer. Cancer Res Treat **2021**;53:773-
644 83
645 24. Chen B, Khodadoust MS, Liu CL, Newman AM, Alizadeh AA. Profiling Tumor Infiltrating Immune
646 Cells with CIBERSORT. Methods Mol Biol **2018**;1711:243-59

647 25. Guedj K, Khallou-Laschet J, Clement M, Morvan M, Gaston AT, Fornasa G, *et al.* M1 macrophages
648 act as LTbetaR-independent lymphoid tissue inducer cells during atherosclerosis-related
649 lymphoid neogenesis. Cardiovasc Res **2014**;101:434-43
650 26. Kang W, Feng Z, Luo J, He Z, Liu J, Wu J, *et al.* Tertiary Lymphoid Structures in Cancer: The
651 Double-Edged Sword Role in Antitumor Immunity and Potential Therapeutic Induction
652 Strategies. Front Immunol **2021**;12:689270
653 27. Goc J, Germain C, Vo-Bourgais TK, Lupo A, Klein C, Knockaert S, *et al.* Dendritic cells in tumor-
654 associated tertiary lymphoid structures signal a Th1 cytotoxic immune contexture and license the
655 positive prognostic value of infiltrating CD8+ T cells. Cancer Res **2014**;74:705-15
656 28. Coppola D, Nebozhyn M, Khalil F, Dai H, Yeatman T, Loboda A, *et al.* Unique ectopic lymph node-
657 like structures present in human primary colorectal carcinoma are identified by immune gene
658 array profiling. Am J Pathol **2011**;179:37-45
659 29. Fernandez-Avila L, Castro-Amaya AM, Molina-Pineda A, Hernandez-Gutierrez R, Jave-Suarez LF,
660 Aguilar-Lemarroy A. The Value of CXCL1, CXCL2, CXCL3, and CXCL8 as Potential Prognosis
661 Markers in Cervical Cancer: Evidence of E6/E7 from HPV16 and 18 in Chemokines Regulation.
662 Biomedicines **2023**;11
663 30. de Chaisemartin L, Goc J, Damotte D, Validire P, Magdeleinat P, Alifano M, *et al.* Characterization
664 of chemokines and adhesion molecules associated with T cell presence in tertiary lymphoid
665 structures in human lung cancer. Cancer Res **2011**;71:6391-9
666 31. Liu Y, Cruikshank WW, O'Loughlin T, O'Reilly P, Center DM, Kornfeld H. Identification of a CD4
667 domain required for interleukin-16 binding and lymphocyte activation. J Biol Chem
668 **1999**;274:23387-95
669 32. Lynch EA, Heijens CA, Horst NF, Center DM, Cruikshank WW. Cutting edge: IL-16/CD4
670 preferentially induces Th1 cell migration: requirement of CCR5. Journal of immunology
671 **2003**;171:4965-8
672 33. Kuo P, Tuong ZK, Teoh SM, Frazer IH, Mattarollo SR, Leggatt GR. HPV16E7-Induced Hyperplasia
673 Promotes CXCL9/10 Expression and Induces CXCR3(+) T-Cell Migration to Skin. J Invest Dermatol
674 **2018**;138:1348-59
675 34. Liang YK, Deng ZK, Chen MT, Qiu SQ, Xiao YS, Qi YZ, *et al.* CXCL9 Is a Potential Biomarker of
676 Immune Infiltration Associated With Favorable Prognosis in ER-Negative Breast Cancer. Front
677 Oncol **2021**;11:710286
678 35. Li Z, Liu J, Li L, Shao S, Wu J, Bian L, *et al.* Epithelial mesenchymal transition induced by the
679 CXCL9/CXCR3 axis through AKT activation promotes invasion and metastasis in tongue squamous
680 cell carcinoma. Oncol Rep **2018**;39:1356-68
681 36. Li M, He L, Zhu J, Zhang P, Liang S. Targeting tumor-associated macrophages for cancer
682 treatment. Cell Biosci **2022**;12:85
683 37. Zhang XF, Zhang XL, Wang YJ, Fang Y, Li ML, Liu XY, *et al.* The regulatory network of the
684 chemokine CCL5 in colorectal cancer. Ann Med **2023**;55:2205168
685 38. Aldinucci D, Borghese C, Casagrande N. The CCL5/CCR5 Axis in Cancer Progression. Cancers
686 (Basel) **2020**;12
687 39. Xu J, Shi Q, Lou J, Wang B, Wang W, Niu J, *et al.* Chordoma recruits and polarizes tumor-
688 associated macrophages via secreting CCL5 to promote malignant progression. J Immunother
689 Cancer **2023**;11
690 40. Cambien B, Richard-Fiardo P, Karimdjee BF, Martini V, Ferrua B, Pitard B, *et al.* CCL5
691 neutralization restricts cancer growth and potentiates the targeting of PDGFRbeta in colorectal
692 carcinoma. PloS one **2011**;6:e28842

693 41. Dieu-Nosjean MC, Antoine M, Danel C, Heudes D, Wislez M, Poulot V*, et al.* Long-term survival
694 for patients with non-small-cell lung cancer with intratumoral lymphoid structures. J Clin Oncol
695 **2008**;26:4410-7
696 42. Karapetyan L, AbuShukair HM, Li A, Knight A, Al Bzour AN, MacFawn IP*, et al.* Expression of
697 lymphoid structure-associated cytokine/chemokine gene transcripts in tumor and protein in
698 serum are prognostic of melanoma patient outcomes. Front Immunol **2023**;14:1171978
699 43. Li C, Hua K. Dissecting the Single-Cell Transcriptome Network of Immune Environment
700 Underlying Cervical Premalignant Lesion, Cervical Cancer and Metastatic Lymph Nodes. Front
701 Immunol **2022**;13:897366
702 44. Chauhan J, Grandits M, Palhares L, Mele S, Nakamura M, Lopez-Abente J*, et al.* Anti-cancer pro-
703 inflammatory effects of an IgE antibody targeting the melanoma-associated antigen chondroitin
704 sulfate proteoglycan 4. Nat Commun **2023**;14:2192
705 45. Yao X, Chen W, Zhao C, Wei L, Hu Y, Li M*, et al.* Naturally acquired HPV antibodies against
706 subsequent homotypic infection: A large-scale prospective cohort study. Lancet Reg Health West
707 Pac **2021**;13:100196
708 46. Beachler DC, Jenkins G, Safaeian M, Kreimer AR, Wentzensen N. Natural Acquired Immunity
709 Against Subsequent Genital Human Papillomavirus Infection: A Systematic Review and Meta-
710 analysis. The Journal of infectious diseases **2016**;213:1444-54
711 47. Safaeian M, Castellsague X, Hildesheim A, Wacholder S, Schiffman MH, Bozonnat MC*, et al.* Risk
712 of HPV-16/18 Infections and Associated Cervical Abnormalities in Women Seropositive for
713 Naturally Acquired Antibodies: Pooled Analysis Based on Control Arms of Two Large Clinical
714 Trials. The Journal of infectious diseases **2018**;218:84-94
715 48. Gorvel L, Olive D. Tumor associated macrophage in HPV(+) tumors: Between immunosuppression
716 and inflammation. Semin Immunol **2022**;65:101671
717 49. Pittet MJ, Michielin O, Migliorini D. Clinical relevance of tumour-associated macrophages. Nat
718 Rev Clin Oncol **2022**;19:402-21
719 50. Park MD, Silvin A, Ginhoux F, Merad M. Macrophages in health and disease. Cell **2022**;185:4259-
720 79
721 51. van Vlerken-Ysla L, Tyurina YY, Kagan VE, Gabrilovich DI. Functional states of myeloid cells in
722 cancer. Cancer Cell **2023**;41:490-504
723 52. Del Prete A, Salvi V, Soriani A, Laffranchi M, Sozio F, Bosisio D*, et al.* Dendritic cell subsets in
724 cancer immunity and tumor antigen sensing. Cell Mol Immunol **2023**;20:432-47
725 53. Truxova I, Kasikova L, Hensler M, Skapa P, Laco J, Pecen L*, et al.* Mature dendritic cells correlate
726 with favorable immune infiltrate and improved prognosis in ovarian carcinoma patients. J
727 Immunother Cancer **2018**;6:139
728 54. Minohara K, Imai M, Matoba T, Wing JB, Shime H, Odanaka M*, et al.* Mature dendritic cells
729 enriched in regulatory molecules may control regulatory T cells and the prognosis of head and
730 neck cancer. Cancer Sci **2023**;114:1256-69
731 55. Duraiswamy J, Turrini R, Minasyan A, Barras D, Crespo I, Grimm AJ*, et al.* Myeloid antigen-
732 presenting cell niches sustain antitumor T cells and license PD-1 blockade via CD28
733 costimulation. Cancer Cell **2021**;39:1623-42 e20
734 56. Haque A, Moriyama M, Kubota K, Ishiguro N, Sakamoto M, Chinju A*, et al.* CD206(+) tumor-
735 associated macrophages promote proliferation and invasion in oral squamous cell carcinoma via
736 EGF production. Sci Rep **2019**;9:14611
737 57. Yagi T, Baba Y, Okadome K, Kiyozumi Y, Hiyoshi Y, Ishimoto T*, et al.* Tumour-associated
738 macrophages are associated with poor prognosis and programmed death ligand 1 expression in
739 oesophageal cancer. Eur J Cancer **2019**;111:38-49

740 58. Li Z, Maeda D, Yoshida M, Umakoshi M, Nanjo H, Shiraishi K, *et al.* The intratumoral distribution
741 influences the prognostic impact of CD68- and CD204-positive macrophages in non-small cell
742 lung cancer. Lung Cancer **2018**;123:127-35
743 59. Schweer D, McAtee A, Neupane K, Richards C, Ueland F, Kolesar J. Tumor-Associated
744 Macrophages and Ovarian Cancer: Implications for Therapy. Cancers (Basel) **2022**;14
745 60. Petitprez F, de Reynies A, Keung EZ, Chen TW, Sun CM, Calderaro J, *et al.* B cells are associated
746 with survival and immunotherapy response in sarcoma. Nature **2020**;577:556-60
747 61. Helmink BA, Reddy SM, Gao J, Zhang S, Basar R, Thakur R, *et al.* B cells and tertiary lymphoid
748 structures promote immunotherapy response. Nature **2020**;577:549-55
749 62. Wang L, Guo W, Guo Z, Yu J, Tan J, Simons DL, *et al.* PD-L1-expressing tumor-associated
750 macrophages are immunostimulatory and associate with good clinical outcome in human breast
751 cancer. Cell Rep Med **2024**;5:101420
752 63. Zhang Y, Wang N, Ding M, Yang Y, Wang Z, Huang L, *et al.* CD40 Accelerates the Antigen-Specific
753 Stem-Like Memory CD8(+) T Cells Formation and Human Papilloma Virus (HPV)-Positive Tumor
754 Eradication. Front Immunol **2020**;11:1012
755 64. Ceglia V, Zurawski S, Montes M, Kroll M, Bouteau A, Wang Z, *et al.* Anti-CD40 Antibody Fused to
756 CD40 Ligand Is a Superagonist Platform for Adjuvant Intrinsic DC-Targeting Vaccines. Front
757 Immunol **2021**;12:786144
758 65. Vitale LA, Thomas LJ, He LZ, O'Neill T, Widger J, Crocker A, *et al.* Development of CDX-1140, an
759 agonist CD40 antibody for cancer immunotherapy. Cancer Immunol Immunother **2019**;68:233-45
760 66. Labiano S, Roh V, Godfroid C, Hiou-Feige A, Romero J, Sum E, *et al.* CD40 Agonist Targeted to
761 Fibroblast Activation Protein alpha Synergizes with Radiotherapy in Murine HPV-Positive Head
762 and Neck Tumors. Clin Cancer Res **2021**;27:4054-65
763 67. Nywening TM, Wang-Gillam A, Sanford DE, Belt BA, Panni RZ, Cusworth BM, *et al.* Targeting
764 tumour-associated macrophages with CCR2 inhibition in combination with FOLFIRINOX in
765 patients with borderline resectable and locally advanced pancreatic cancer: a single-centre,
766 open-label, dose-finding, non-randomised, phase 1b trial. Lancet Oncol **2016**;17:651-62
767 68. Dunbar KJ, Karakasheva TA, Tang Q, Efe G, Lin EW, Harris M, *et al.* Tumor-Derived CCL5 Recruits
768 Cancer-Associated Fibroblasts and Promotes Tumor Cell Proliferation in Esophageal Squamous
769 Cell Carcinoma. Mol Cancer Res **2023**;21:741-52
770 69. Zhai T, Mitamura T, Wang L, Kubota SI, Murakami M, Tanaka S, *et al.* Combination therapy with
771 bevacizumab and a CCR2 inhibitor for human ovarian cancer: An in vivo validation study. Cancer
772 Med **2023**;12:9697-708
773 70. Pellizzari G, Hoskin C, Crescioli S, Mele S, Gotovina J, Chiaruttini G, *et al.* IgE re-programs
774 alternatively-activated human macrophages towards pro-inflammatory anti-tumoural states.
775 EBioMedicine **2019**;43:67-81
776 71. Dong K, Chen W, Pan X, Wang H, Sun Y, Qian C, *et al.* FCER1G positively relates to macrophage
777 infiltration in clear cell renal cell carcinoma and contributes to unfavorable prognosis by
778 regulating tumor immunity. BMC Cancer **2022**;22:140
779 72. Sautes-Fridman C, Verneau J, Sun CM, Moreira M, Chen TW, Meylan M, *et al.* Tertiary Lymphoid
780 Structures and B cells: Clinical impact and therapeutic modulation in cancer. Semin Immunol
781 **2020**;48:101406

782

783 **Declarations:**

784 *Ethics approval and consent to participate*

785 Human cervical tumor samples were obtained from patients, who were included in the
786 prospective XAC-03 (NCT02875990) and GC-Bio-IPC (NCT01977274) clinical trials, conducted
787 from 2013 to 2023. The XAC-30 and GC-Bio_IPC trials were approved by the institutional review
788 board (Comité d'Orientation Stratégique (COS), Marseille, France) of the Paoli-Calmettes
789 Institute and the Assistance Publique des Hopitaux de Marseille (AP-HM), respectively. In
790 accordance with the Declaration of Helsinki, written informed consent was obtained from all
791 patients.

792

793 *Data Availability*

794 All data presented in the manuscript are original results and are available upon
795 reasonable request to daniel.olive@inserm.fr. The publicly available TCGA CESC dataset, used
796 for TLS cell enrichment and signature associated survival, is available on the TCGA data portal
797 https://portal.gdc.cancer.gov/projects/TCGA-CESC.

798

799

800

801 *Competing interests*

802 D.O. is a cofounder and shareholder of Imcheck Therapeutics, Alderaan Biotechnology,
803 Emergence Therapeutics, and Stealth IO, which did not take part in any part of the manuscript.

804 RS declares to have received research grants from Astra-Zeneca, consulting fees from
805 GSK and EISAI, and non-financial support from MSD, Astra-Zeneca, GSK, and Novartis, none of
806 which participated to this study.

807 EL declares to have received consulting fees from GSK and MSD, none of which
808 participated to this study.

809 Other authors do not have any conflits of interest to declare.

810

811 *Acknowledgements*

We would like to thank the translational histopathology ICEP platform (CRCM, Marseille, France) for destocking patient FFPE blocks, and cutting the slides. We would like to thank Manon Richaud and Françoise Mallet at the CRCM Cytometry platform (CRCM, Marseille, France) for their insights in panel design and access to cytometers. Editorial assistance for English language improvement was provided by Angloscribe, Calvisson, France.

Author contributions

L.G. and D.O. designed the project. L.G., J.S., C.D., and N.B., dissociated tumor samples. L.G., M.S.R., N.B., A.B.A., and J.S. performed the phenotyping experiment. L.G., N.B., and O.Q. performed the soluble factor dosages and analysis. M.P. performed the IF staining and acquisitions. E.B performed and interpreted LASSO analysis. M.P. and L.G. performed spatial analyses. L.G. analyzed CyTOF and flow cytometry experiments. X.C., R.S., E.L., and O.Q. enrolled patients in the studies, performed patient follow-up, extracted clinical data and obtained tumor samples. S.G., L.G. and S.F. performed the statistical analyses on cervical tumors. L.G. and A.S.C. performed the statistical analyses and the MFA analysis of clinical data. L.G., M.P. and M.C.D.N. interpreted the data. M.C.D.N. and D.O. supervised the project. L.G. drafted the manuscript and designed the figures. J.A.N aided in manuscript corrections. All authors reviewed the manuscript and provided insights. We declare that all authors contributed to the study and accept accountability of the data herein, and fulfil the authorship criteria.

Consent for publication

Not applicable

Funding

Not applicable

Additional information

Correspondence and requests for materials should be addressed to Laurent Gorvel (laurent.gorvel@inserm.fr) or Daniel Olive (daniel.olive@inserm.fr).

Figure Legends:

Figure 1: TLS are associated with B cell density and dendritic cell activation as well as with a higher inflammatory profile in cervical tumors. A, Immunohistochemistry (IHC) for DC-LAMP, CD3, CD20 and CD21 was performed on n=34 cervical tumor FFPE samples. TLS were detected in 17/34 samples. **B**, Dot plots show DC density against the TLS maturation classification **C**, Dot plots show B cell density against the TLS maturation classification **D**, Dot plots show TLS counts against the TLS maturation classification in the 34 FFPE samples. **E**, Images show a representative TLS, stained by multiplex IHC for CD20, CD3, DAPI, DC-LAMP, CD21 and PNAD. **F**, soluble factors were detected in tumor supernatants by Luminex. Dot plot represent the concentration of each proteins in healthy cervix, TLS^{-}, $TLS^{imm.}$ and $TLS^{mat.}$ tumors in pg/ml. Statistical analyses were performed using Kruskal-Wallis test followed by a Dunn, multiple comparison post-test (*p-val<0.05, **p-val<0.01, *** p-val<0.005, **** p-val<0.001).

Figure 2: TLS^{+} tumors exhibit a higher B cell infiltrate characterized by an enrichment of plasmablasts in the stromal compartment and exacerbated IgG presence. A, Manual gating of tumor infiltrating B cell subpopulations in n= 6 TLS^{-} and n=3 TLS^{+} samples. **B**, B cell absolute count normalized by gram of tumor sample. **C**, B cell subpopulation frequencies in n= 6 TLS^{-} and n=3 TLS^{+} samples. **D**, Memory B cell phenotyping in n= 6 TLS^{-} and n=3 TLS^{+} samples. Frequencies of parent population are shown only when parent population contained enough events (>30 cells). **E**, Multiplex IF was performed for CD20, CD138, CD3, CD8, and PanCk on TLS^{-} (left, n=6) and TLS^{+} (right, n=6) FFPE samples. **F**, B cells ($CD20^{+}CD138^{-}$) and ASCs ($CD138^{+}CD20^{+}$, $CD138^{+}CD20^{-}PanCk^{-}$) were quantified in the tumor ($PanCk^{+}$) compartment. **G**, B cells ($CD20^{+}CD138^{-}$) and ASCs ($CD138^{+}CD20^{+}$, $CD138^{+}CD20^{-}PanCk^{-}$) were quantified in the stromal ($PanCk^{-}$) compartment. **H**, immunoglubulins were measured in healthy cervix, TLS^{-}, $TLS^{imm.}$ and $TLS^{mat.}$ supernatants. Statistical analyses were performed using Kruskal-Wallis test followed by a Dunn, multiple comparison post-test (*p-val<0.05, **p-val<0.01, *** p-val<0.005).

867 **Figure 3: CD163$^+$ macrophages and mature cDC2 are enriched in TLS$^+$ cervical tumors. A**, Tumor
868 infiltrating myeloid cells were analyzed by mass cytometry on n= 14 samples, h-SNE and density
869 clustering. Clusters were annotated according to the expression of markers in **Supplementary Table 5**. **B**,
870 TAMs were gated and quantified in n=14 samples and plotted according to the presence or absence of
871 TLS. **C**, multiplex IHC was performed to identify CD163$^+$CD68$^+$ and CD163$^-$CD68$^+$ TAMs in TLS$^+$ (n=6) and
872 TLS$^-$ (n=6) tumors. Representative images are shown (top) and cell quantities were assessed (bottom). **D**,
873 cDC2, CD1a^{hi} LCs and CD1a^{lo} DCs were gated and quantified in n=14 samples and plotted according to the
874 presence or absence of TLS. **E**, multiplex IHC was performed to identify mDCs (DC-LAMP$^+$CD1a$^-$), mLCs
875 (DC-LAMP$^+$CD1a$^+$) and iLCs (DC-LAMP$^-$CD1a$^+$) in TLS$^+$ and TLS$^-$ tumors. Representative images are shown
876 (top) and cell quantities were assessed in the tumor nest (center) and stroma (bottom). Statistical
877 analyses were performed using Mann-Whitney test (*p-val<0.05)

878

879 **Figure 4: LASSO analysis highlights macrophage and DC activation in TLS$^+$ tumors. A**, Individual marker
880 frequencies (PD-L1, CD40, CD86 …) was assessed in each myeloid cell subtype identified by CyTOF per
881 patient (n=14). Then, data were filtered to retain frequencies in cell cluster with a count > to 30 cells as
882 well as an average expression > to 10%. This led to 101 identified variables, which were then analyzed by
883 LASSO to identify specific variables to either TLS$^-$ or TLS$^+$ TME. **B**, LASSO selected variables associated
884 with TLS$^+$ TME. **C**, LASSO identified variables associated with TLS$^-$ TME. **D**, univariate analysis of the 101
885 variables. Volcano plot shows distribution of variables in TLS$^-$ and TLS$^+$ TME.

886

887 **Figure 5: Spatial analysis reveals increased interactions between mDCs and CD8$^+$ T cells, which exhibit**
888 **higher diversity in TLS$^+$ tumors. A**, multiplex IF was performed to identify mDCs (DC-LAMP$^+$CD1a$^-$),
889 mCD1a$^+$ DCs (DC-LAMP$^+$CD1a$^+$) and nmCD1a$^+$ DCs (DC-LAMP$^-$CD1a$^+$) in TLS$^+$ (n=6) and TLS$^-$ (n=6) tumors.
890 **B**, schematic representation of proximity analysis. **C**, mCD1a^{hi} proximity to CD8$^+$ T cells was quantified
891 within 10µm, 10-20µm and 20-30µm range in TLS$^-$ and TLS$^+$ tumors. **D**, mDCs proximity to CD8$^+$ T cells
892 was quantified within 10µm, 10-20µm and 20-30µm range in TLS$^-$ and TLS$^+$ tumors. **E**, CD8$^+$ T cells subsets
893 (naïve, EM, CM, TEMRA) were gated and quantified by mass cytometry (n=14). Absolute counts are
894 shown as dot-plots. **F**, CD4$^+$ T cells subsets (naïve, EM, CM, TEMRA) were gated and quantified by mass
895 cytometry. Absolute counts are shown as dot-plots. **G**, CD4$^+$ T cell analysis by h-SNE and density
896 clustering. The heatmap represent maker expression per cluster and each cluster annotation. Violin plot
897 represent the frequency of each cluster in TLS$^+$ and TLS$^-$ samples. "Checkpoint$^-$" EM CD4$^+$T cells did not

898 express any immune checkpoint present in our panel. **F**, $CD8^+$ T cell analysis by h-SNE and density
899 clustering. The heatmap represent maker expression per cluster and each cluster annotation. Violin plot
900 represent the frequency of each cluster in TLS^+ and TLS^- samples. "Markerless" $CD8^+$ T cell did not
901 express any of the markers present in our Lymphocyte mass cytometry panel other dans CD3 and CD8.
902 Statistical analyses were performed using Mann-Whitney test (*p-val<0.05).

903

904 **Figure 6: TLS^+ tumors with high B cell and DC density are associated with improved prognosis. A.** MFA
905 was performed on 34 patients and highlighted TLS maturation, FIGO stages and Relapses and death as
906 significant discriminating factors. **B,** Waterfall chart displays the follow up of n=34 patients, annotated in
907 function of the absence of TLS (red, TLS^-), presence of immature TLS^+ (orange) or mature TLS (blue).
908 Crosses represent deaths and R represent relapses. **C,** Kaplan-Meier plot represent relapse free survival
909 of patients in the 3 groups defined in **B**. **D**, Immune cell enrichment algorithm CIBERSORTx was used to
910 investigate TIL infiltrate in TCGA CESC cohort (306 patients). Kaplan-Meier curves were generated for
911 scored TLS related cell types ($CD8^+$ Tcells, B cells and activated DCs). A high score of enrichment for these
912 cell types was annotated TLS^+ (green) and lower scores were annotated TLS^- (black). *p<0.05. Coppola et
913 al. (**E**) and Goc et al. (**F**) gene signatures were applied to the CESC dataset from TCGA. The signatures
914 were then scored using quartiles (**E**) or median (**F**) and Kaplan-Meier curves were generated. Statistical
915 differences were calculated using the Log-rank test. *p-val<0.05, **p-val<0.01, ***p-val<0.005, ****p-
916 val<0.001.

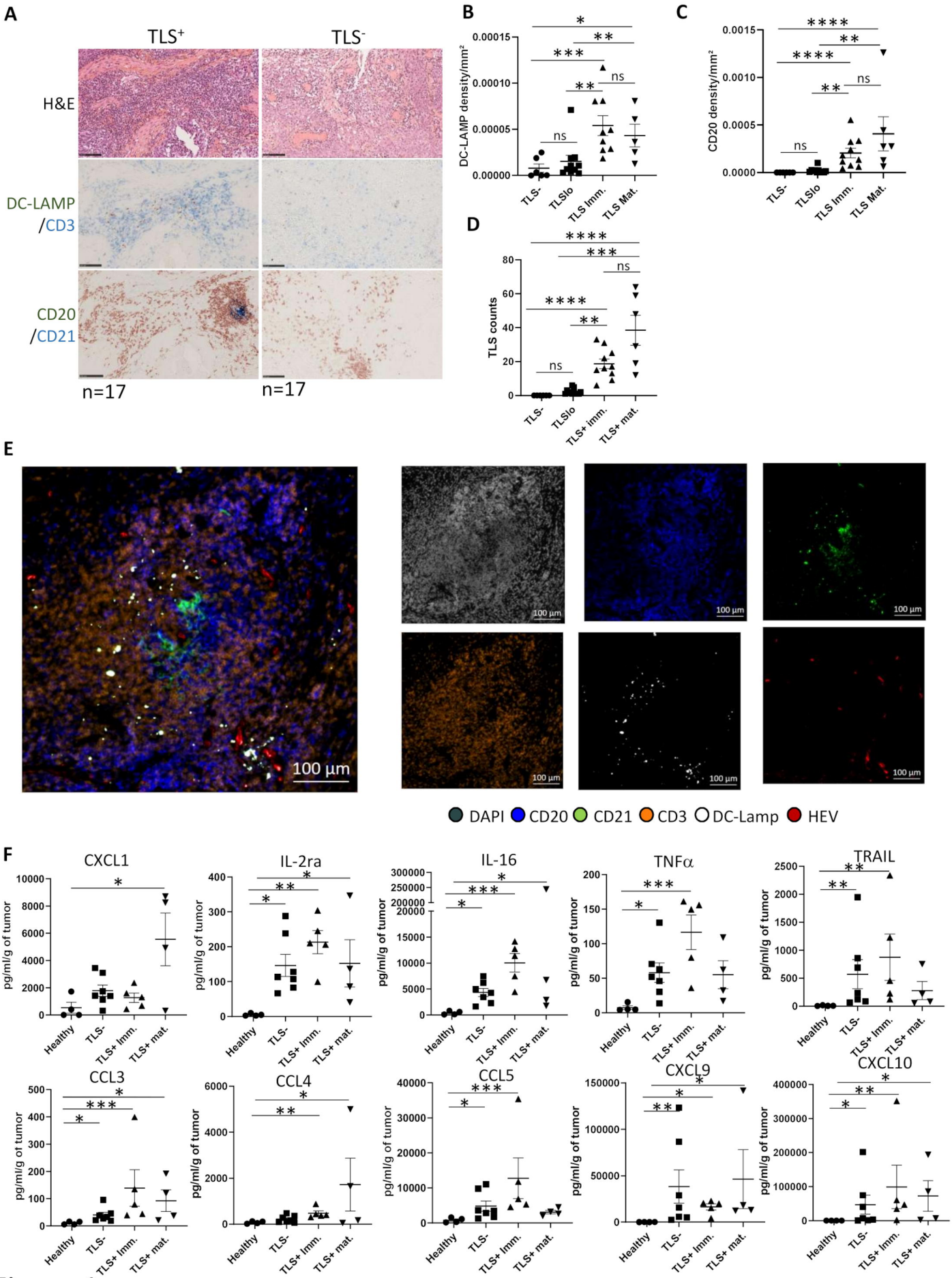
A
TLS+
TLS-
H&E
DC-LAMP /CD3
CD20 /CD21
n=17
n=17
B
DC-LAMP density/mm²
TLS-
TLSlo
TLS Imm.
TLS Mat.
C
CD20 density/mm²
D
TLS counts
TLS+ imm.
TLS+ mat.
E
100 µm
DAPI
CD20
CD21
CD3
DC-Lamp
HEV
F
CXCL1
IL-2ra
IL-16
TNFα
TRAIL
CCL3
CCL4
CCL5
CXCL9
CXCL10
pg/ml/g of tumor
Healthy
TLS-
TLS+ Imm.
TLS+ mat.

Figure 1

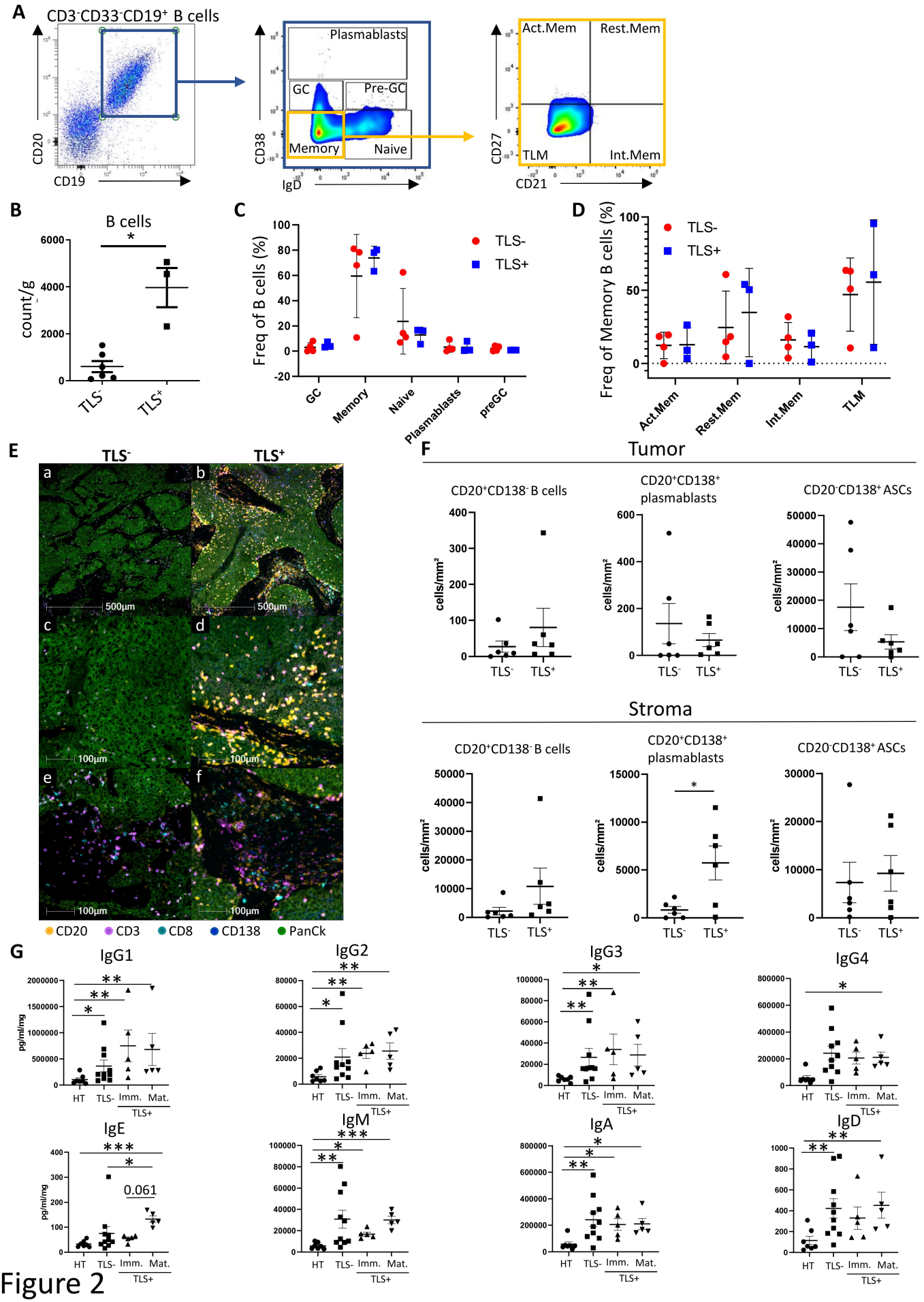
A
CD3-CD33-CD19+ B cells
CD20
CD19
Plasmablasts
GC
Pre-GC
Memory
Naive
CD38
IgD
Act.Mem
Rest.Mem
TLM
Int.Mem
CD27
CD21
B
B cells
count/g
TLS-
TLS+
C
Freq of B cells (%)
TLS-
TLS+
GC
Memory
Naive
Plasmablasts
preGC
D
Freq of Memory B cells (%)
TLS-
TLS+
Act.Mem
Rest.Mem
Int.Mem
TLM
E
TLS-
TLS+
500µm
100µm
CD20
CD3
CD8
CD138
PanCk
F
Tumor
CD20+CD138- B cells
CD20+CD138+ plasmablasts
CD20-CD138+ ASCs
cells/mm²
Stroma
G
IgG1
IgG2
IgG3
IgG4
IgE
IgM
IgA
IgD
pg/ml/mg
HT
TLS-
Imm.
Mat.
TLS+
0.061

Figure 2

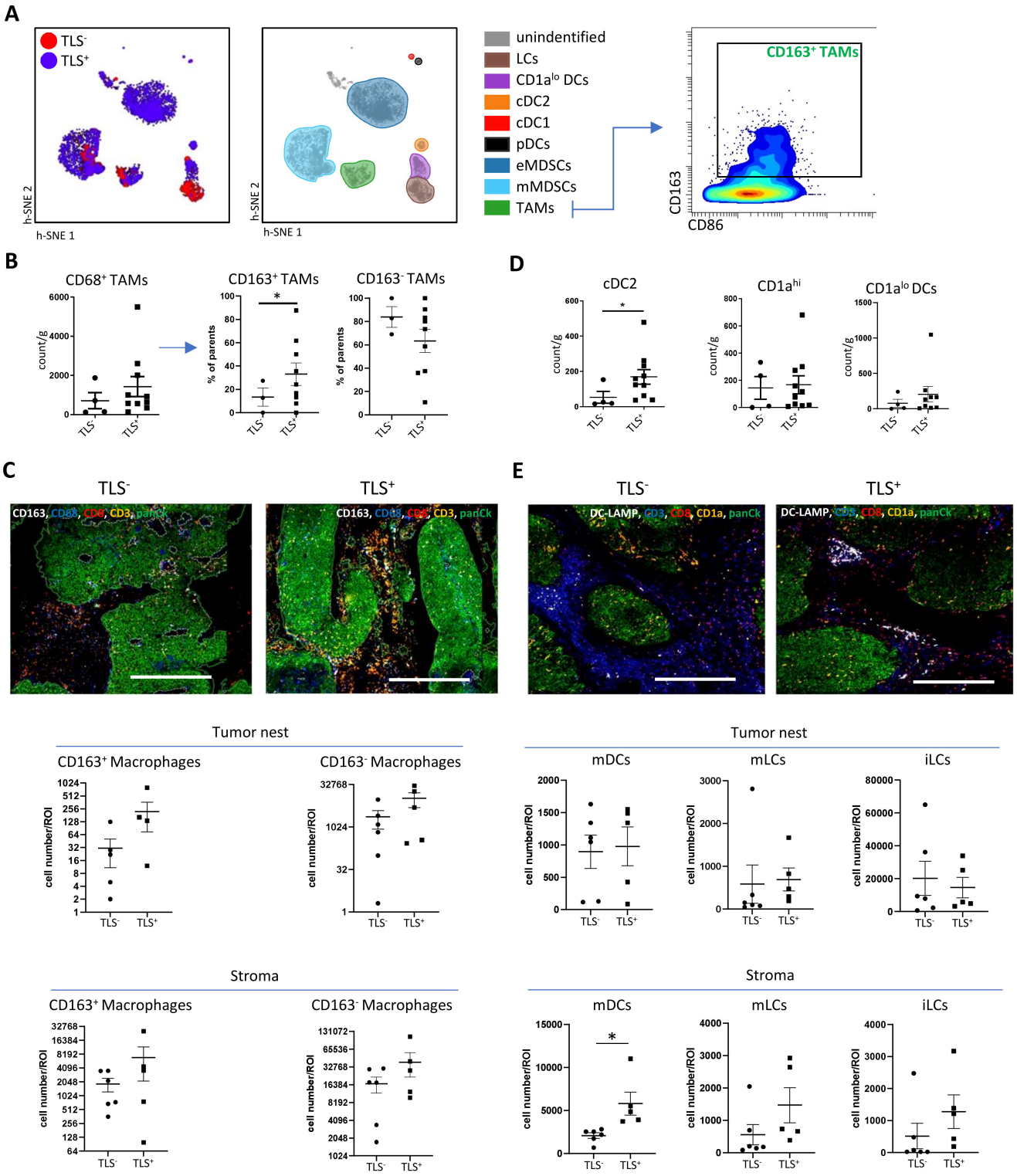
A
TLS-
TLS+
h-SNE 1
h-SNE 2
unindentified
LCs
CD1a^lo DCs
cDC2
cDC1
pDCs
eMDSCs
mMDSCs
TAMs
CD163+ TAMs
CD163
CD86
B
CD68+ TAMs
CD163+ TAMs
CD163- TAMs
count/g
% of parents
D
cDC2
CD1a^hi
CD1a^lo DCs
C
TLS-
TLS+
CD163, CD68, CD8, CD3, panCk
E
DC-LAMP, CD3, CD8, CD1a, panCk
Tumor nest
CD163+ Macrophages
CD163- Macrophages
mDCs
mLCs
iLCs
Stroma
cell number/ROI

Figure 3

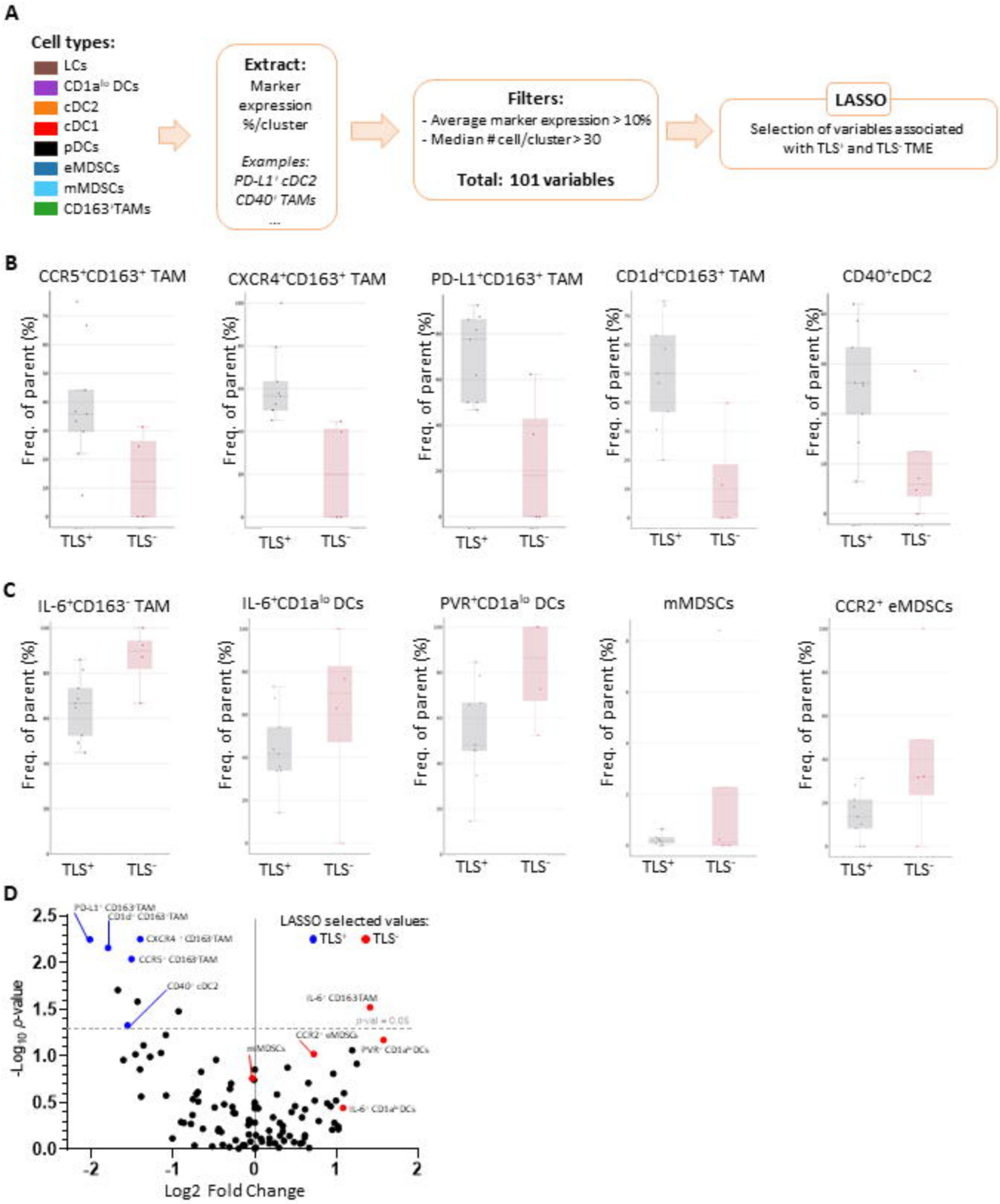
A
Cell types:
LCs
CD1a^{lo} DCs
cDC2
cDC1
pDCs
eMDSCs
mMDSCs
CD163$^+$TAMs
Extract:
Marker expression %/cluster
Examples:
PD-L1$^+$ cDC2
CD40$^+$ TAMs
...
Filters:
- Average marker expression > 10%
- Median # cell/cluster > 30
Total: 101 variables
LASSO
Selection of variables associated with TLS$^+$ and TLS$^-$ TME
B
CCR5$^+$CD163$^+$ TAM
CXCR4$^+$CD163$^+$ TAM
PD-L1$^+$CD163$^+$ TAM
CD1d$^+$CD163$^+$ TAM
CD40$^+$cDC2
Freq. of parent (%)
TLS$^+$
TLS$^-$
C
IL-6$^+$CD163$^-$ TAM
IL-6$^+$CD1a^{lo} DCs
PVR$^+$CD1a^{lo} DCs
mMDSCs
CCR2$^+$ eMDSCs
Freq. of parent (%)
TLS$^+$
TLS$^-$
D
LASSO selected values:
TLS$^+$
TLS$^-$
PD-L1$^+$ CD163$^+$TAM
CD1d$^+$ CD163$^+$TAM
CXCR4$^+$ CD163$^+$TAM
CCR5$^+$ CD163$^+$TAM
CD40$^+$ cDC2
IL-6$^+$ CD163TAM
p-val = 0.05
CCR2$^+$ eMDSCs
mMDSCs
PVR$^+$ CD1a^{lo} DCs
IL-6$^+$ CD1a^{lo} DCs
-Log$_{10}$ p-value
Log2 Fold Change
2.5
2.0
1.5
1.0
0.5
0.0
-2
-1
0
1
2

Figure 4

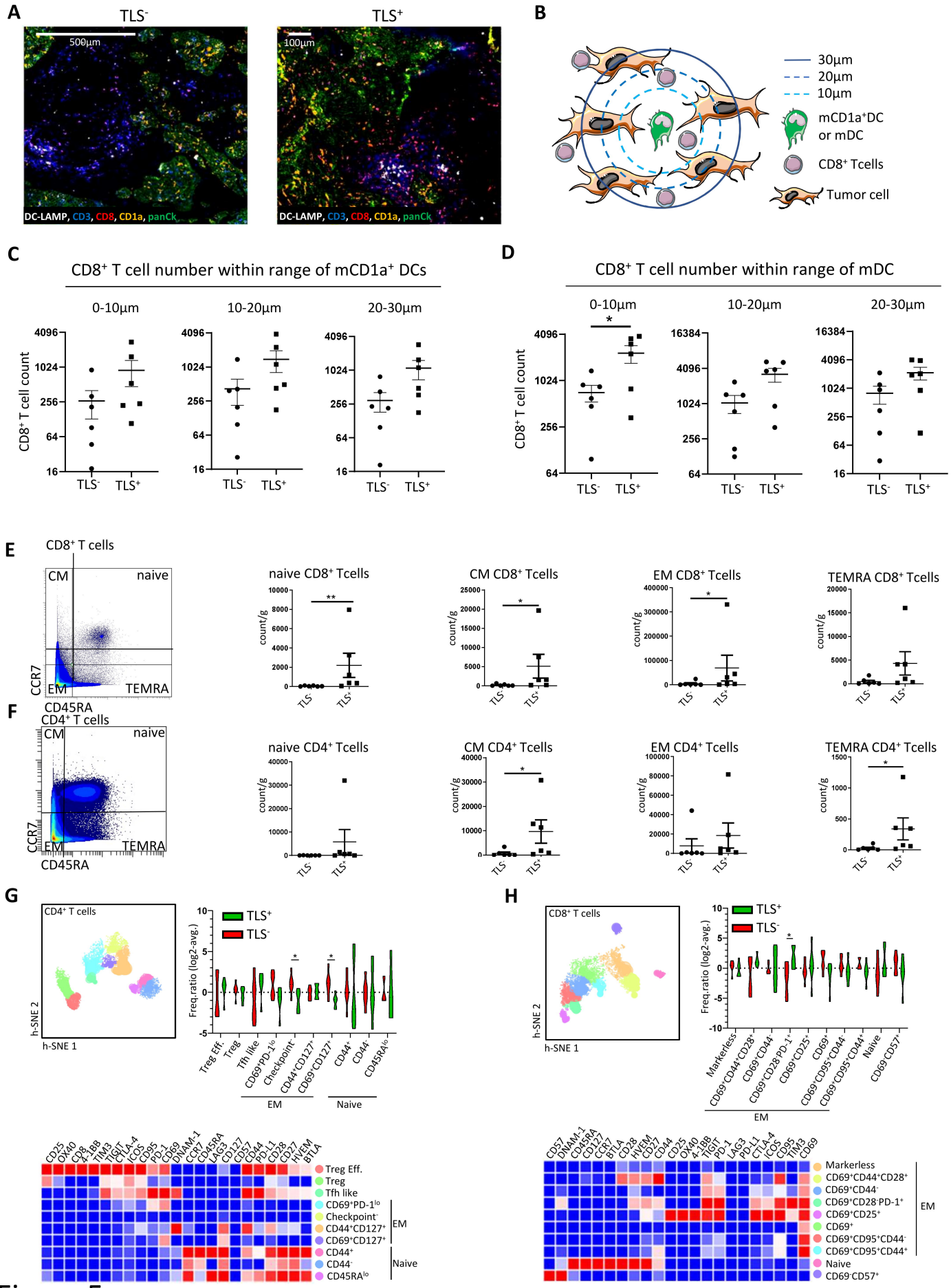
A
TLS-
TLS+
500µm
100µm
DC-LAMP, CD3, CD8, CD1a, panCk
B
30µm
20µm
10µm
mCD1a+DC or mDC
CD8+ Tcells
Tumor cell
C
CD8+ T cell number within range of mCD1a+ DCs
0-10µm
10-20µm
20-30µm
CD8+ T cell count
TLS-
TLS+
D
CD8+ T cell number within range of mDC
E
CD8+ T cells
CM
naive
EM
TEMRA
CCR7
CD45RA
naive CD8+ Tcells
CM CD8+ Tcells
EM CD8+ Tcells
TEMRA CD8+ Tcells
count/g
F
CD4+ T cells
naive CD4+ Tcells
CM CD4+ Tcells
EM CD4+ Tcells
TEMRA CD4+ Tcells
G
CD4+ T cells
h-SNE 1
h-SNE 2
Freq.ratio (log2-avg.)
Treg Eff.
Treg
Tfh like
CD69+PD-1lo
Checkpoint-
CD44+CD127+
CD69+CD127+
CD44+
CD44-
CD45RAlo
EM
Naive
H
CD8+ T cells
Markerless
CD69+CD44+CD28+
CD69+CD44-
CD69+CD28-PD-1+
CD69+CD25+
CD69+
CD69+CD95+CD44-
CD69+CD95+CD44+
CD69-CD57+

Figure 5

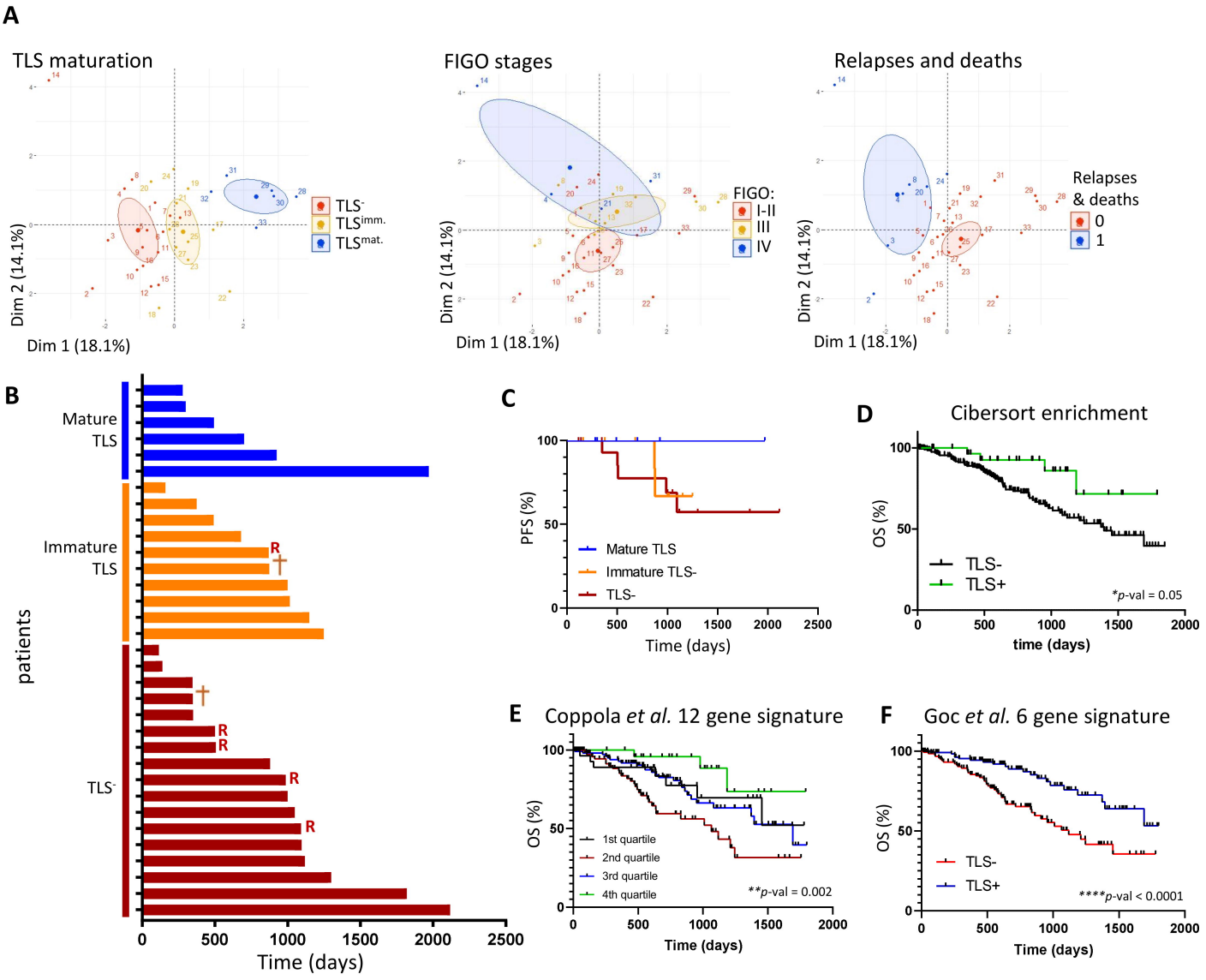
A
TLS maturation
FIGO stages
Relapses and deaths
Dim 1 (18.1%)
Dim 2 (14.1%)
TLS-
TLSimm.
TLSmat.
FIGO:
I-II
III
IV
Relapses & deaths
0
1
B
Mature TLS
Immature TLS
TLS-
patients
Time (days)
C
PFS (%)
Mature TLS
Immature TLS-
TLS-
Time (days)
D
Cibersort enrichment
OS (%)
TLS-
TLS+
*p-val = 0.05
time (days)
E
Coppola et al. 12 gene signature
OS (%)
1st quartile
2nd quartile
3rd quartile
4th quartile
**p-val = 0.002
Time (days)
F
Goc et al. 6 gene signature
OS (%)
TLS-
TLS+
****p-val < 0.0001
Time (days)

Figure 6

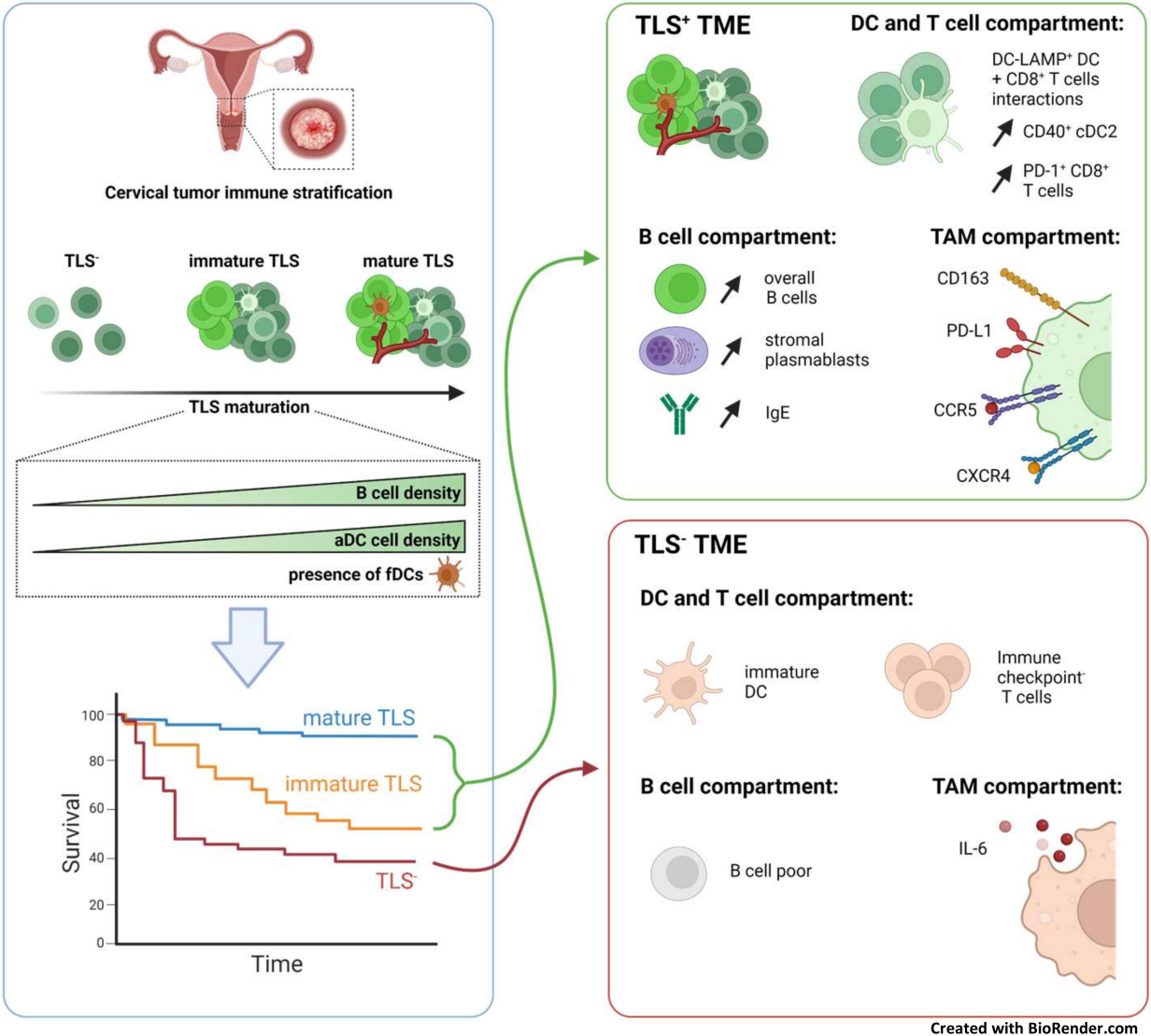
Cervical tumor immune stratification
TLS⁻
immature TLS
mature TLS
TLS maturation
B cell density
aDC cell density
presence of fDCs
Survival
Time
100
80
60
40
20
0
mature TLS
immature TLS
TLS⁻
TLS⁺ TME
DC and T cell compartment:
DC-LAMP⁺ DC + CD8⁺ T cells interactions
CD40⁺ cDC2
PD-1⁺ CD8⁺ T cells
B cell compartment:
overall B cells
stromal plasmablasts
IgE
TAM compartment:
CD163
PD-L1
CCR5
CXCR4
TLS⁻ TME
DC and T cell compartment:
immature DC
Immune checkpoint⁻ T cells
B cell compartment:
B cell poor
TAM compartment:
IL-6
Created with BioRender.com

Table 1: Clinical characteristics of cervical cancer patients

		Tumor samples*	Healthy samples
Characteristic	**-**	**n=34**	**n=5**
Age, median (range)	*Current (years)*	58 (37-80)	
	At diagnosis (years)	53 (32-77)	
Histology, n	*SCC***	28	*NA*
	*ADK***	5	*NA*
	*Other***	*1*	*NA*
FIGO stages, n	*IB1*	4	*NA*
	IIA1	2	*NA*
	IIA2	1	*NA*
	IIB	14	*NA*
	IIIA	1	*NA*
	IIIB	3	*NA*
	IIIC1	5	*NA*
	IVA	2	*NA*
	IVB	2	*NA*
Emboli, n	*Positive*	3	0
	Negative	31	5
LN invasion, n	*Positive*	14	0
	Negative	20	5
Adverse events, n	**Metastasis**	4	0
	Relapses	5	0
	Deaths	2	0
Treatments, n	**RCT*** + Barytherapy**	26	*NA*
	Radio-Chemotherapy	5	*NA*
	Chemotherapy	1	*NA*
	Barytherapy	2	*NA*

**Note: cervical tumors are considered 100% HPV+*
*** Note: SCC: squamous cell carcinoma; ADK: adenocarcinoma; Other: mixed origins, serous, clear cell carcinomas*
****Note: RCT: Radio-chemotherapy*

Patient	DC density (cell/mm²)	B cell density (cell/mm²)	TLS counts	fDCs in B cell zone	TLS maturity scoring
GC1282	8.05122E-05	0.000332744	33	NO	IMMATURE
GC1322	1.8465E-05	0.000177513	15	NO	IMMATURE
GC1471	0.00010261	6.02821E-05	13	NO	IMMATURE
XACI11	2.87553E-05	0.000133947	17	NO	IMMATURE
XACI16	2.75875E-05	0.000238909	16	NO	IMMATURE
XACN12	4.92789E-05	0.000551579	22	NO	IMMATURE
XACN14	8.10343E-05	0.000322344	9	NO	IMMATURE
XACN2	3.68913E-05	4.13829E-05	31	NO	IMMATURE
XACN3	0.000116616	7.35915E-05	25	NO	IMMATURE
XACN7	4.69993E-05	0.000114184	6	NO	IMMATURE
GC1389	8.07186E-05	0.000274351	48	YES	MATURE
GC1468	1.26599E-05	0.000127847	59	YES	MATURE
XACC1	3.64324E-05	0.000276118	64	YES	MATURE
XACN11	2.53324E-05	0.000443208	29	YES	MATURE
XACN15	6.09574E-05	6.25658E-05	19	YES	MATURE
XACN8	9.5982E-05	0.001264506	12	YES	MATURE
GC1323	2.89623E-06	2.13661E-05	3	NO	NEGATIVE
GC1358	1.82409E-05	2.31198E-05	2	NO	NEGATIVE
GC1364	3.59181E-07	0	0	NO	NEGATIVE
GC1374	7.8166E-06	1.87018E-05	6	YES	NEGATIVE
GC1393/XACI15	1.05998E-05	2.03246E-06	1	NO	NEGATIVE
GC1409	1.95797E-05	0.000100016	1	NO	NEGATIVE
GC1483	1.06908E-05	8.33479E-06	2	NO	NEGATIVE

XACl06	0	0	0	NO	NEGATIVE
XACl07	3.48074E-06	0	0	NO	NEGATIVE
XACl14	0	0	0	NO	NEGATIVE
XACN10	1.88341E-05	0	0	NO	NEGATIVE
XACN13	2.3648E-06	2.38441E-06	1	NO	NEGATIVE
XACN16	7.10688E-05	6.31852E-06	2	NO	NEGATIVE
XACN4	6.30323E-06	1.95452E-06	1	NO	NEGATIVE
XACN5	6.98434E-06	1.71416E-05	5	NO	NEGATIVE
XACN6	2.35104E-05	2.47682E-05	1	NO	NEGATIVE
XACN9	4.19883E-06	1.44199E-05	2	NO	NEGATIVE

Table 2: TLS scoring parameters and values